J Adv Ceram

Research Article

Preparation of porous mullite ceramics composed entirely of overlapping and interlocking mullite whiskers through whisker *in-situ* growth

Ruoyu Zhang[1,†], Jingjing Li[2,†], Ziqing Wang[1], Chenchen Qi[3], Jing Zhuo[1], Yange Wan[3], Yajie Zhang[1], Hongli Liu[1], Bo Xiao[4], Mingchao Wang[1,2,✉]

Cite this article: Zhang R, Li J, Wang Z, et al. *J Adv Ceram* 2025, **14**(4): 9221055. https://doi.org/10.26599/JAC.2025.9221055

ABSTRACT: A novel porous mullite ceramic with overlapping and interlocking mullite whiskers was prepared using *in-situ* whisker growth technology. Without the use of any pore-foaming agents, the formation of a porous structure was facilitated by the atomic rearrangement of Al_2O_3 and SiO_2 catalyzed with MoO_3. The effects of the molar ratio of Al_2O_3 to SiO_2, MoO_3 content, sintering time, and sintering temperature on the structure and properties of $(xAl_2O_3{\cdot}ySiO_2)_m(MoO_3)_n$-*T*-*t* (*T* = sintering temperature, and *t* = sintering duration) ceramics were comprehensively studied. The molar ratio of Al_2O_3 to SiO_2 had a more significant effect on the morphology of the whiskers, while the other three conditions generally promote whisker growth. Under conditions of $x : y = 3 : 1.8$, $m : n = 9 : 1$, $T = 1300$ °C, and $t = 3$ h, $(3Al_2O_3{\cdot}1.8SiO_2)_9(MoO_3)_1$-1300 °C-3 h ceramics exhibited a satisfactory compressive strength of 4.81 MPa at a density of 0.76 g/cm³. Microstructural analysis revealed that a multi-level reinforcement structure was obtained by the interlaced distribution of tiny and large whiskers, significantly increasing the crack deflection area and enhancing the crack deflection resistance when resisting external forces. After 100 thermal shock cycles between room temperature and 1300 °C, the compressive strength retention rate was 77.13%. In addition, the multi-scale whisker-overlapping structure also has a high specific surface area (1.83 m²/g), high porosity (74.18%), and small pore size (7.44 μm). The thermal conductivity was as low as 0.260 W/(m·K), and the ceramic maintained a rear-side temperature below 200 °C when subjected to a 1300 °C butane flame. In addition, the regulatory mechanism between parameters, structure, and properties was analyzed in detail, providing data support for research on porous materials.

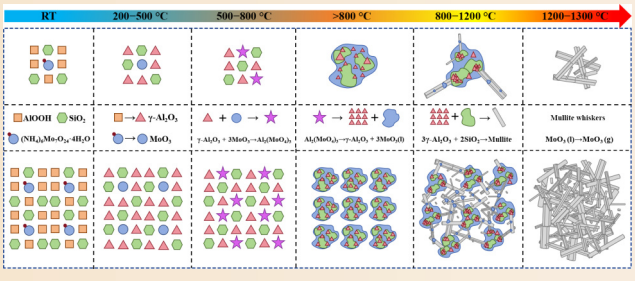

KEYWORDS: porous ceramics; *in-situ* growth; full whisker construction; one-time sintering; thermal insulation performance

1 Introduction

Porous insulating ceramics, with their low density, excellent mechanical properties, and thermal insulation capabilities [1–3], have become essential materials in aerospace, significantly enhancing aircraft's thermal protection [4,5]. They also play crucial roles in high-performance ceramic matrix composites, offering superior high-temperature and wear resistance [6]. Their extensive use in construction, transportation, industrial equipment, and power industries has improved energy efficiency and extended component life [7–9], demonstrating their significant value across various sectors.

Typical porous insulating ceramics include mullite, zirconia, silicate, and diatomaceous earth [10–12]. Compared with other materials, mullite porous ceramics exhibit excellent high-temperature resistance and good thermal insulation performance and are less susceptible to chemical corrosion [13–16]. Traditional methods for preparing mullite porous ceramics result in insufficient strength, making them prone to cracking or damage under significant external force or mechanical impact [17,18]. Additionally, these materials are susceptible to thermal shock cracking under severe temperature fluctuations, which can reduce their reliability and durability [19].

Whisker toughening is an effective method for enhancing the strength and toughness of porous ceramics [20,21]. The toughening mechanisms include crack deflection, whisker pull-

† Ruoyu Zhang and Jingjing Li contributed equally to this work.

[1] Aviation Engineering Institute, Civil Aviation University of China, Tianjin 300300, China. [2] College of Science, Civil Aviation University of China, Tianjin 300300, China. [3] Department of Safety Engineering, Civil Aviation University of China, Tianjin 300300, China. [4] Binzhou Beicheng Construction Engineering Materials Testing Co., Ltd., Binzhou 256602, China.

✉ Corresponding author. E-mail: mingchaowang0@163.com

Received: December 1, 2024; Revised: February 26, 2025; Accepted: February 26, 2025

out, and bridging, which allow the material to maintain good mechanical properties at high temperatures [22]. This method primarily consists of two toughening techniques: direct addition [23] and *in-situ* growth [24]. Direct addition involves physically mixing whiskers into the ceramic matrix, thereby improving the material's mechanical properties through the interaction between the whiskers and matrix [25–27]. However, this method has the drawbacks of high cost and long material preparation cycles, and the inserted whiskers may not disperse uniformly, potentially creating weak points within the material and affecting the overall strength. The *in-situ* growth method directly synthesizes mullite whiskers within the ceramic matrix [28–30]. Li *et al.* [31] prepared self-reinforced porous mullite ceramics using the starch consolidation method, where *in-situ* synthesized mullite whiskers formed an interlocking structure, resulting in porous mullite ceramics with a bending strength of approximately 100 MPa and an apparent porosity of approximately 55% at 1550 °C. The second method provides better toughening effects than the first method and ensures more uniform whisker dispersion. However, achieving a good bond between the matrix and the whiskers still requires additional steps, and perfect integration is complicated. When mullite whiskers are grown in a ceramic matrix, there are still many mismatches between the whiskers and the ceramic matrix, especially thermal property mismatches [32]. Such mismatches can lead to cracking and micro-cracking of the material after high-temperature exposure and multiple thermal cycles.

Owing to the excellent toughening effects of whiskers and the unique characteristics of *in-situ* whisker growth, if porous ceramics can be produced using the *in-situ* whisker growth technique, with a structure formed entirely by overlapping or interlocking whiskers, it would effectively address long-standing mismatches between whiskers and the matrix, as well as interface bonding issues. Yang *et al.* [33] used hollow alumina spheres as the primary raw material and active mullite precursor powder as the high-temperature binder to successfully produce porous ceramics with a porosity of 74.9%. The mullite whiskers interacted to form an interlocking structure between the hollow alumina spheres, creating a nearly all-whisker network structure that significantly enhanced the mechanical and thermal insulation properties of the porous ceramics. However, for this type of ceramic, it is still necessary to consider the matching characteristics between the hollow alumina spheres and the whiskers. The presence of hollow alumina spheres within the whiskers can affect the ceramic structure, thereby influencing the increment in ceramic strength. Although this network structure resembles an all-whisker network, it is not truly an all-whisker network structure. Therefore, controlling the whisker growth source and utilizing the *in-situ* growth process to develop novel porous ceramics with fully overlapping and interlocking whiskers has significant research value.

The fully interlocking whisker porous ceramic structure ensures excellent mechanical properties [34,35] and features low density and high compressive strength. Owing to its unique porous characteristics, it can effectively reduce the thermal conductivity and significantly improve the thermal insulation performance [36]. In addition, whisker ceramics, which are composed entirely of whiskers, avoid the subsequent steps of addition and mixing required in traditional whisker-reinforced ceramics, significantly reducing production costs and time consumption. Furthermore, this method allows for precise control over the whisker growth process [37], such as the molar ratio of alumina to silica, catalyst addition, and sintering conditions, all of which impact the growth morphology of whiskers in the ceramics. The precise control of the whisker growth process enables effective regulation of the structural strength, allowing ceramics to be adjusted and optimized according to diverse practical needs and better meeting the specific requirements of different application scenarios. Thus, this work explored changes in the properties of porous ceramics by controlling the raw materials and growth processes.

This study used nano-alumina sol and nano-silica sol as raw materials and ammonium molybdate tetrahydrate as a fluxing agent. Porous ceramics composed of overlapping and interlocking mullite whiskers were prepared using *in-situ* growth technology. The sol-gel method was employed to prepare the whisker growth precursors, which were further transformed into high-performance whiskers via molten salt catalysis. The effects of the molar ratio of alumina to silica, catalyst content, sintering time, and sintering temperature on whisker growth within the ceramics, the structure and composition evolution of ceramics, mechanical properties, and the thermal insulating mechanism were thoroughly investigated. Additionally, the formation mechanism of porous ceramics and the regulatory mechanism between parameters, structure, and properties were analyzed in detail.

In addition to the novelty demonstrated by the structure of porous ceramics, this work's innovation is also reflected in the innovation of preparation methods and forming mechanisms. First, the porous ceramics in this work were prepared by pressureless dry sintering by filling the preformed whisker precursor powder into the mold. Most existing processes for preparing high-strength porous ceramics involve wet preparation, such as preparation of gel bodies by sol. The shrinkage rate during the drying process is high, making it difficult to control in industrial production. Unlike wet methods, dry methods have lower shrinkage rates and are more conducive to controlling component dimensions [38,39]. In addition, the drying method is simple; the preparation cost is low, and the mold utilization rate is high. Second, the generation of porous ceramics in this work is based on the atomic rearrangement of alumina/silica under the action of catalysts without using a foaming agent. The conventional preparation of porous materials generally requires pore-forming agents, such as starch, carbon powder, and PMMA balls. Unmixed pore-forming agents can easily cause large pore sizes or uneven pore structures, making it difficult to ensure product quality. In addition, some pore-forming agents, such as hexadecyltrimethylammonium bromide and sodium dodecyl sulfate (SDS) [40,41], are prone to decompose and release irritating gases, seriously affecting personal safety.

2 Materials and methods

2.1 Sample preparation

Nano-alumina sol (Al_2O_3, 10–20 nm, solid content 15.91 wt%, Jingrui New Materials Co., Ltd., China) was used as the aluminum source, and nano-silica sol (SiO_2, 10–20 nm, solid content 24.65 wt%, Jingrui New Materials Co., Ltd., China) was used as the silicon source. Ammonium molybdate tetrahydrate ($(NH_4)_6Mo_7O_{24}{\cdot}4H_2O$, purity > 99%, Kemiou Chemical Reagents Co., Ltd., China) was employed as the flux agent and catalyst.

The alumina and silica sol were mixed with water, constituting 15–20 wt% of the total solution mass, and stirred thoroughly. Ammonium molybdate was added, and the mixture was continuously stirred for 20 min to obtain a sol-like mullite whisker growth precursor paste. The stoichiometric ratios of Al, Si, and Mo were designated $(xAl_2O_3{\cdot}ySiO_2)_m(MoO_3)_n$, with $x : y$ ratios of 3 : 1.8, 3 : 2, and 3 : 2.2 and $m : n$ ratios of 10 : 0, 9 : 1, 8 : 2, 7 : 3, and 6 : 4. The samples were placed in an oven, dried at 80 °C for

16 h, ground into a powder with a particle size of 320 mesh using a mortar and pestle, weighed to ensure uniform powder mass, and filled into ϕ20 mm × 20 mm alumina molds without compaction. The samples were then dried and sintered in air at different temperatures (1100, 1200, 1300, 1400, and 1500 °C) for various durations (1, 2, and 3 h) to obtain porous ceramics composed of overlapping and interlocking whiskers. The preparation process is shown in Fig. S1 in the Electronic Supplementary Material (ESM), and the prepared samples are shown in Fig. S2 in the ESM.

2.2 Sample characterizations

The compressive performance of porous ceramics was obtained using a microcomputer-controlled electronic universal testing machine (CMT4504, MTS, China) at a constant loading rate of 0.2 mm/min. The bulk density of the ceramics was determined by mass/volume. The compression and resilience properties of the ceramics were determined through a uniaxial compression–decompression tester (CMT4304, Instrumentation Industry Systems (China) Co., Ltd., China) with a set compression rate of 0.02 mm/min. Furthermore, a thermal shock test was conducted at 1300 °C using a GSL-1700X tubular furnace (Hefei Kejing Material Technology Co., Ltd., China). Test samples were directly heated to 1300 °C for 10 min and then transferred to the ambient atmosphere for cooling for 10 min. After undergoing different numbers of thermal cycles, the compressive strength of the ceramics was tested under the same conditions using the CMT4504 machine. For the above tests, five samples (ϕ20 mm × 20 mm) for each kind of ceramic were tested, and the average values were calculated to determine the performance of the porous ceramics.

X-ray diffraction (XRD) patterns were obtained using an X-ray diffractometer (D/Max-2500, Rigaku, Japan, Cu Kα radiation) to analyze the phase composition of the ceramics, with the test samples being powders with a particle size of 320 mesh. The ceramics' mullite proportion was determined through whole-pattern fitting combined with Rietveld refinement analysis of the XRD data. To further understand the structure of the porous ceramics, Brunauer–Emmett–Teller (BET) tests were conducted using ASAP 2460 adsorption apparatus (Micromeritics, USA), with samples degassed under helium conditions at 150 °C for 3 h. The microstructures of the samples were observed through a scanning electron microscope (SEM; S-4800, Hitachi, Japan). The test samples were irregularly shaped blocks with dimensions of approximately 5 mm × 5 mm × 5 mm. The dimensions of whiskers and the pore sizes in ceramics were calculated with Nano Measurer 1.2 software. In addition, the porosities of samples were measured using a porosity density tester (DA-300PM, Guangdong Hongtuo, China) combined with the Archimedes method and water immersion technique. A Fourier transform infrared spectrometer (FTIR; Nicolet iS5, Thermo Scientific, USA) was used to analyze the chemical bonds of ceramics, further revealing their chemical characteristics, with test samples being powders with a particle size of 320 mesh. The thermal reaction process of mullite whisker precursor powder and thermal stability of ceramics from room temperature to 1300 °C were measured using a thermogravimetric analyzer–differential scanning calorimetrer (TG–DSC; STA 449F3, NETZSCH Instruments Manufacturing Co., Germany) under air at 20 °C/min.

Thermal conductivity measurements were conducted on the ceramics using a thermostability analyzer (TPS 2500S, Hot Disk, Sweden), with the test samples having dimensions of ϕ10 mm × 2 mm. A multi-channel temperature inspection instrument (JK4000, Jinke, China) was used to analyze the ability of the ceramics to resist heat conduction when exposed to a 1300 °C flame from a butane torch. Additionally, a thermal infrared imager (LT7-P, Zhejiang Dali Technology Co., Ltd., China) was used to measure the thermal images of ceramics. The test samples for these two tests had dimensions of ϕ16 mm × 16 mm. Additionally, a microcomputer horizontal expansion instrument (HPY-3, Beijing Hengjiu, China) was utilized to obtain the linear expansion of the ceramics during temperature changes, characterizing their physical properties at different temperatures. The test samples had dimensions of 20 mm × 4 mm × 4 mm. Owing to the time-consuming nature of the thermal performance experiment, the performance of each ceramic sample was taken as the average of three samples.

3 Results and discussion

3.1 Composition and structural analysis

3.1.1 *Phase and structural analysis*

Figure 1(a) shows the XRD patterns of $(x\mathrm{Al_2O_3}{\cdot}y\mathrm{SiO_2})_9(\mathrm{MoO_3})_1$ ceramics sintered at 1300 °C for 3 h, with variations in the molar ratio of Al_2O_3 to SiO_2 from 3 : 1.8 to 3 : 2.2. The diffraction peaks included the mullite phase, as well as residual hexagonal γ-Al_2O_3 and tetragonal α-SiO_2 phases. The content of mullite was calculated and is listed in Table 1. Obviously, within a minimal range, the molar ratio of Al_2O_3 to SiO_2 had a relatively small effect on mullite production. When $x : y = 1 : 8$, the generated mullite content reached 88.9% (Table 1). For $x : y = 3 : 2.2$, the amount generated was 91.2%. The difference in mullite production under three conditions was less than 3%. However, with increasing SiO_2 content, the mullite production still increased because under flux conditions, the melting point of SiO_2 decreased, and the reaction activity increased.

Figure 1(b) shows the XRD patterns of $(3\mathrm{Al_2O_3}{\cdot}1.8\mathrm{SiO_2})_m(\mathrm{MoO_3})_n$ ceramics sintered at 1300 °C for 3 h, with variations in the ratio of $m : n$ from 6 : 4 to 10 : 0. As the content of MoO_3 increased, the intensity of the mullite peaks gradually increased, while those of Al_2O_3 and SiO_2 peaks weakened progressively. At $m : n = 10 : 0$, without adding any catalyst, only a small amount of Al_2O_3 reacted with SiO_2 to produce trace amounts of mullite. The percentage of mullite was only 28.0% (Table 1). As the content of MoO_3 increased, the mullite content gradually increased, reaching 97.5% at $m : n = 6 : 4$.

Figure 1(c) shows the XRD patterns of $(3\mathrm{Al_2O_3}{\cdot}1.8\mathrm{SiO_2})_9(\mathrm{MoO_3})_1$ ceramics sintered at 1300 °C, with variations in sintering time from 1 to 3 h. The mullite content increased from 82.7% to 88.9%. Figure 1(d) shows the XRD patterns of $(3\mathrm{Al_2O_3}{\cdot}1.8\mathrm{SiO_2})_9(\mathrm{MoO_3})_1$ ceramics sintered for 3 h, with variations in the sintering temperature ranging from 1100 to 1500 °C. At 1100 °C, many small and weak diffraction peaks of Al_2O_3 and SiO_2 were observed, and the nucleation and growth of mullite began at approximately 1100 °C [42]. As the sintering temperature increased, the intensity of the mullite phase diffraction peaks rapidly increased. At 1500 °C, the intensity of the mullite diffraction peaks was notably strong, and the obtained mullite phase contained no apparent impurity phases. Notably, the aluminum/silicon ratio in mullite is not strictly stoichiometric at 3 : 1, and the content of Al_2O_3 is generally in the range of 72–78 wt% [43]. For $m : n = 3 : 1.8$, the content of Al_2O_3 was 73.9 wt%, meeting the conditions for mullite formation. As shown in Table 1, the percentage of mullite rose from 47.7% at 1100 °C to 98.1% at 1500 °C.

In addition, infrared spectroscopy analysis was conducted on all

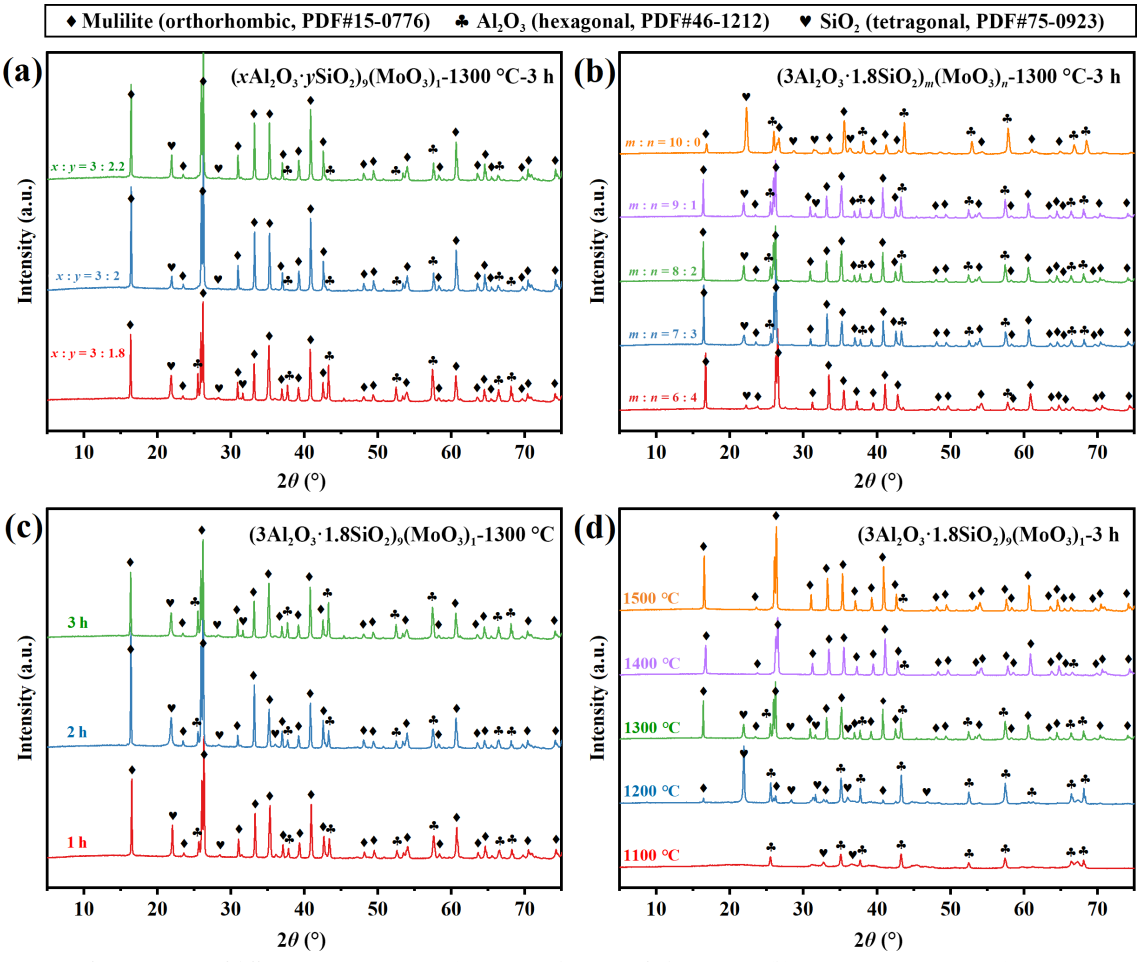

Fig. 1 Comparison of XRD patterns of different porous ceramics: (a) varying molar ratios of Al_2O_3 to SiO_2, (b) varying MoO_3 contents, (c) varying sintering time, and (d) varying sintering temperatures.

Table 1 Mullite content and structural parameters of different porous ceramics

Molar ratio of Al_2O_3 to SiO_2 (x : y)	MoO_3 content (m : n)	Sintering time (h)	Sintering temperature (°C)	Mullite percentage (wt%)	Whisker length (μm)	Specific surface area (m^2/g)	Pore size (μm)	Porosity (%)
3 : 1.8	9 : 1	3	1300	88.9	6.18 (tiny) 20.08 (large)	1.83	7.44	74.18
3 : 2.0	9 : 1	3	1300	90.3	34.86	1.71	9.85	66.22
3 : 2.2	9 : 1	3	1300	91.2	13.56	2.08	3.92	69.77
3 : 1.8	6 : 4	3	1300	97.5	36.71	1.29	1.37	34.46
3 : 1.8	7 : 3	3	1300	95.7	32.54	1.32	1.75	37.73
3 : 1.8	8 : 2	3	1300	92.2	34.24	1.80	8.96	73.96
3 : 1.8	10 : 0	3	1300	28.0	—	1.19	0.87	26.34
3 : 1.8	9 : 1	1	1300	82.7	5.93	2.16	2.23	68.78
3 : 1.8	9 : 1	2	1300	84.1	14.67	2.07	4.31	71.54
3 : 1.8	9 : 1	3	1100	47.7	—	1.13	0.92	27.51
3 : 1.8	9 : 1	3	1200	81.8	15.63	1.92	5.39	76.36
3 : 1.8	9 : 1	3	1400	94.2	31.31	1.30	1.83	45.77
3 : 1.8	9 : 1	3	1500	98.1	33.29	1.28	1.56	36.89

the samples listed in Table 2, with detailed analyses in the ESM. As shown in Fig. S3 in the ESM, the absorption bands of various samples clearly did not significantly differ, primarily reflecting the presence of Al–O and Si–O bonds in the ceramics. Overall, the most crucial influence on compositional evolution was exerted by the addition of ammonium molybdate and sintering temperature, followed by sintering time and molar ratio of Al_2O_3 to SiO_2.

Figure 2 presents the micro-morphology of porous ceramics under different preparation conditions. Except for $(3Al_2O_3{\cdot}1.8SiO_2)_{10}(MoO_3)_0$-1300 °C-3 h ceramics, all the other samples were composed of overlapping and interlocking whiskers. Specifically, Figs. 2(a)–2(c) present the morphological variations in ceramics with different molar ratios of Al_2O_3 to SiO_2. For $(3Al_2O_3{\cdot}1.8SiO_2)_9(MoO_3)_1$-1300 °C-3 h ceramics ($x$: y = 3 : 1.8), built with a combination of large and tiny whiskers, the tiny whiskers were interspersed among the larger ones, with aspect

Table 2 Basic parameters of porous ceramics in this work

Sample	Chemical formula	Sintering temperature (°C)	Sintering time (h)	Compressive strength (MPa)	Density (g/cm³)	Specific strength (N·m/kg)
Sam-1	$(3Al_2O_3{\cdot}1.8SiO_2)_9(MoO_3)_1$	1300	3	4.81	0.76	6328.9
Sam-2	$(3Al_2O_3{\cdot}1.8SiO_2)_9(MoO_3)_1$	1300	1	1.49	0.83	1795.2
Sam-3	$(3Al_2O_3{\cdot}1.8SiO_2)_9(MoO_3)_1$	1300	2	2.13	0.79	2696.2
Sam-4	$(3Al_2O_3{\cdot}1.8SiO_2)_{10}(MoO_3)_0$	1300	3	0.42	1.13	371.7
Sam-5	$(3Al_2O_3{\cdot}1.8SiO_2)_8(MoO_3)_2$	1300	3	0.84	0.70	1200.0
Sam-6	$(3Al_2O_3{\cdot}2SiO_2)_9(MoO_3)_1$	1300	3	2.34	0.89	2629.2
Sam-7	$(3Al_2O_3{\cdot}2.2SiO_2)_9(MoO_3)_1$	1300	3	0.62	0.85	729.4
Sam-8	$(3Al_2O_3{\cdot}1.8SiO_2)_9(MoO_3)_1$	1200	3	2.78	0.96	2895.8
Sam-9	$(3Al_2O_3{\cdot}1.8SiO_2)_9(MoO_3)_1$	1400	3	1.73	0.91	1901.1

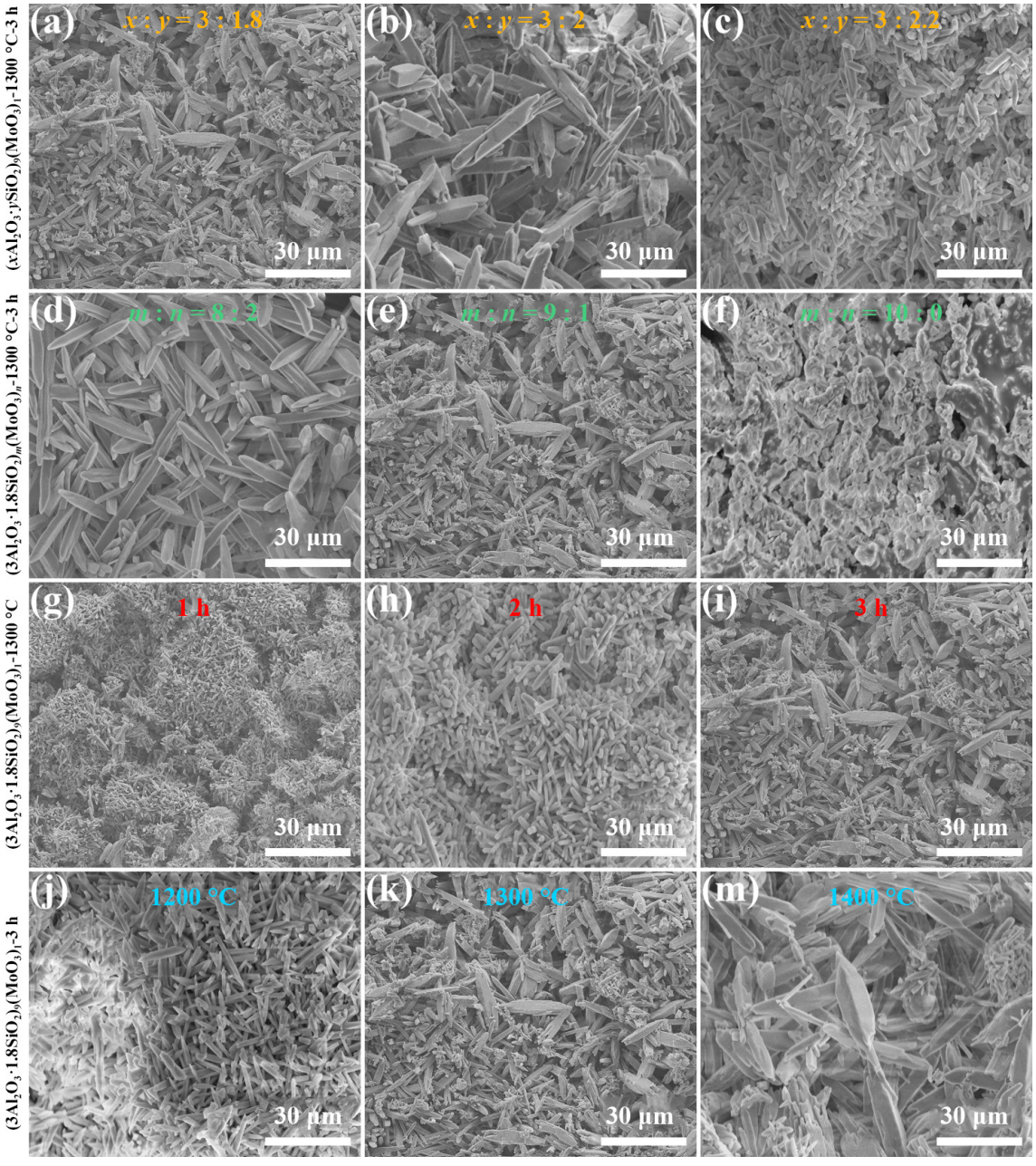

Fig. 2 Low-magnification SEM images of $(xAl_2O_3{\cdot}ySiO_2)_9(MoO_3)_1$-1300 °C-3 h ((a) $x : y = 3 : 1.8$; (b) $x : y = 3 : 2$, (c) $x : y = 3 : 2.2$), $(3Al_2O_3{\cdot}1.8SiO_2)_m(MoO_3)_n$-1300 °C-3 h ((d) $m : n = 8 : 2$; (e) $m : n = 9 : 1$; (f) $m : n = 10 : 0$), $(3Al_2O_3{\cdot}1.8SiO_2)_m(MoO_3)_n$-1300 °C for different hours ((g) 1 h; (h) 2 h; (i) 3 h), and $(3Al_2O_3{\cdot}1.8SiO_2)_9(MoO_3)_1$-3 h treated at different temperatures ((j) 1200 °C; (k) 1300 °C; (m) 1400 °C) (high-magnification images are shown in Fig. S4 in the ESM).

ratios concentrated approximately 4.0–4.6. The average length of tiny whiskers was approximately 6.18 μm, while the average length of large-sized whiskers was approximately 20.08 μm. For $(3Al_2O_3{\cdot}2SiO_2)_9(MoO_3)_1$-1300 °C-3 h ceramics ($x : y = 3 : 2$), the

size of whiskers was significantly larger than that of the former, and the average length was 34.86 μm, with an aspect ratio of 6.52. The locking effect between these large whiskers was pronounced. For $(3Al_2O_3{\cdot}2.2SiO_2)_9(MoO_3)_1$-1300 °C-3 h ceramic ($x : y$ = 3 : 2.2), owing to the increase in SiO_2 content, the amount of SiO_2 melted in the liquid MoO_3 flux also increased, increasing the number of nucleation points of mullite whiskers, thus resulting in a small size and large quantity of mullite whiskers. The average length of whiskers in Fig. 2(c) was only approximately 13.56 μm, with an aspect ratio of 4.9. The number of whiskers in Fig. 2(c) was greater than 400, while that in Fig. 2(b) was only 207. In addition, the residual SiO_2 acted as an adhesive phase, closely adhering to the smaller whiskers to form a stacked structure. Therefore, the overlapping effect in this structure ($x : y$ = 3 : 2.2) is not significant. Among the three types of porous structures mentioned above, the porosity was highest when large and tiny whiskers were cross-distributed ($x : y$ = 3 : 1.8) at approximately 74.18%. The porosity of the porous ceramic with the largest whisker size ($x : y$ = 3 : 2) is the lowest, at approximately 66.22%. The differences in these structures directly impacted their mechanical and thermal properties. Overall, the porous ceramics were composed of whiskers with no noticeable particle residue. However, XRD revealed that all three ceramics contained residual Al_2O_3 and SiO_2. It was evident that Al_2O_3 and SiO_2 played a role in whisker interconnection and adhesion within the structure, effectively improving the connection strength of the overlapped nodes.

Figures 2(d)–2(f) illustrate the morphological variations in ceramics with different MoO_3 contents. For $(3Al_2O_3{\cdot}1.8SiO_2)_8(MoO_3)_2$-1300 °C-3 h ceramics ($m : n$ = 8 : 2), the whiskers exhibited the best morphology, with an aspect ratio reaching 7.74 and a high uniformity with an average length of 34.24 μm. The porosity was approximately 73.96%. For $(3Al_2O_3{\cdot}1.8SiO_2)_{10}(MoO_3)_0$-1300 °C-3 h ceramics ($m : n$ = 10 : 0), the morphology was bulk-like with almost no whisker formation, and its porosity was only 26.34%. When $m : n$ = 6 : 4 and $m : n$ = 7 : 3 (Fig. S5 in the ESM), the width of the whiskers significantly increased, the whiskers partially transformed into large columnar grains, and the porous structure considerably deteriorated.

Figures 2(g)–2(i) show the morphological variations of ceramics with different sintering time. For $(3Al_2O_3{\cdot}1.8SiO_2)_9(MoO_3)_1$-1300 °C-1 h ceramics (1 h), the whiskers were relatively tiny (5.93 μm) and closely interlocked, with an aspect ratio of 9.35. Therefore, although mullite formed and whiskers began to grow in shorter sintering time, the degree of whisker development was not yet high. For $(3Al_2O_3{\cdot}1.8SiO_2)_9(MoO_3)_1$-1300 °C-2 h ceramics (2 h), the length of the whiskers significantly increased to 14.67 μm, and the length-to-diameter ratio was approximately 5.3. When the sintering time was increased to 3 h, the adhesion between the whiskers generated some large whiskers, and many tiny whiskers were distributed in the voids where the large whiskers overlapped. It was assumed that the residual Al_2O_3 and SiO_2 were the intermediate phases of whisker adhesion. This structure, which was formed by the coordinated overlapping of large and tiny whiskers, not only increased the porosity but also improved the mechanical properties of the structure.

Figures 2(j), 2(k), and 2(m) (together with Fig. S6 in the ESM) show the morphological variations in $(3Al_2O_3{\cdot}1.8SiO_2)_9(MoO_3)_1$-3 h ceramics with different sintering temperatures. At 1100 °C, no whiskers were generated (Figs. S6(a) and S6(c) in the ESM). After heat treatment at 1200 °C, whiskers with a length of 15.63 μm (aspect ratio: 4.76) were formed and showed an initial overlapping structure. The porosity reached a maximum of 76.36% at 1200 °C. The morphology at 1200 °C for 3 h (Fig. 2(j)) was similar to that at 1300 °C for 2 h (Fig. 2(h)), but the porosity was higher at low temperatures. Subsequently, the extension of time or increase in temperature promoted the growth of tiny whiskers into large whiskers. At 1300 °C, the residual SiO_2 and Al_2O_3 between the whiskers further reacted to form mullite, with some forming tiny mullite whiskers and others merging with the surrounding whiskers to form large whiskers. The final structure was a mixture of large and tiny whiskers that overlapped, and the porosity of ceramics decreased to 74.18%. However, after treatment at 1400 °C, some whiskers significantly increased into rod-like grains (Fig. 2(m)), and the porosity was only 45.77%. After treatment at 1500 °C, the porous structure fully transformed into a large-grain stacking structure (Figs. S6(b) and S6(d) in the ESM), and the porosity decreased to 36.89%.

TEM tests were conducted on whiskers from porous $(xAl_2O_3{\cdot}ySiO_2)_9(MoO_3)_1$-1300 °C-3 h ceramics with different aluminum/silicon ratios, as shown in Fig. 3. The whisker sizes in Fig. 3 corresponded well to the sizes shown in Fig. 2. The selected area electron diffraction (SAED) diagrams in the insets of Fig. 3 confirmed that the mullite whiskers were monocrystalline. The tips of the three types of whiskers were relatively flat without spherical droplets, proving that the growth mechanism of mullite whiskers was reaction precipitation in molten salt (solid (S)–liquid (L)–S) without the involvement of gas phase. For whiskers with $x : y$ = 3 : 1.8, the lattice spacing along the growth direction of the whisker was 0.558 nm, which corresponded to the (110) crystal plane of mullite, so the whisker grew along the [110] direction. For whiskers with $x : y$ = 3 : 2 and 3 : 2.2, their lattice spacings were 0.287 and 0.288 nm, respectively, corresponding to the (240) crystal plane of mullite, indicating that the whiskers grew along the [240] direction. Therefore, the molar ratio of Al_2O_3 to SiO_2 affected the growth morphology of mullite whiskers and the growth direction of whiskers. Although the reduction of SiO_2 is not conducive to the formation of mullite, the surface energy of the (110) plane of mullite is the highest, and high surface energy accelerates the growth of this crystal plane [42]. Therefore, the trend of the whisker of $x : y$ = 3 : 1.8 growing along the [110] direction was attributed mainly to the high surface energy of the (110) plane.

In addition, a quantitative analysis of porous ceramics with different preparation conditions was also conducted, and the adsorption–desorption curves exhibited type II adsorption isotherms (large pore materials), as shown in Fig. S7 in the ESM. For ceramics with different $x : y$ ratios, the ceramics with $x : y$ = 3 : 2.2 showed the strongest adsorption capacity, with the highest specific surface area (2.08 m^2/g) and the smallest pore size (3.92 μm). For ceramics with different $m : n$ ratios, the ceramics with $m : n$ = 9 : 1 and 8 : 2 showed better adsorption capacities, which is consistent with their porous structure, as shown by the SEM results. The other three ceramics had almost no hysteresis loops in their adsorption–desorption curves because of the absence of their porous structure. For ceramics sintered for different durations at 1300 °C, the adsorption–desorption tests revealed that their specific surface area gradually decreased with time, from 2.16 m^2/g at 1 h to 1.83 m^2/g at 3 h. The pore size increased from 2.23 to 7.44 μm. These results were consistent with the microstructural changes observed via SEM. For ceramics sintered at different temperatures, the ceramics sintered at 1200 °C had the highest specific surface area of 1.92 m^2/g. The above quantitative results were consistent with the qualitative SEM results.

3.1.2 *TG–DSC analysis*

To evaluate the thermal reaction mechanism of the precursors,

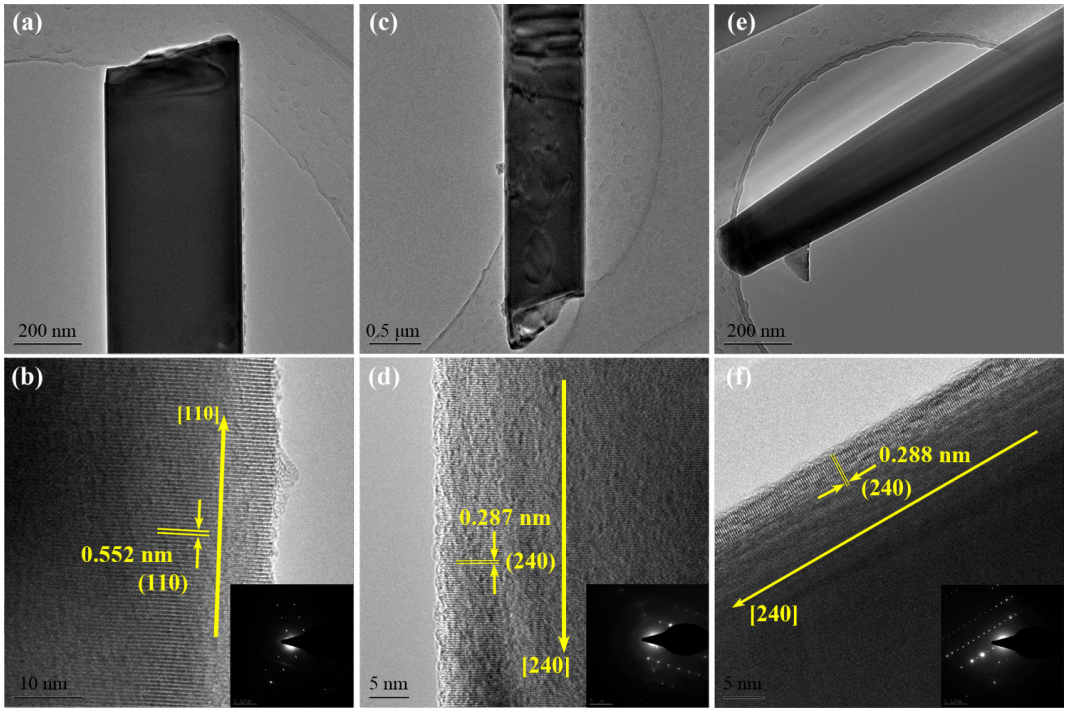

Fig. 3 TEM analysis of mullite whiskers from different $(xAl_2O_3{\cdot}ySiO_2)_9(MoO_3)_1$-1300 °C-3 h ceramics: (a, b) $x : y = 3 : 1.8$; (c, d) $x : y = 3 : 2$; (e, f) $x : y = 3 : 2.2$.

TG–DSC was performed on $(3Al_2O_3{\cdot}1.8SiO_2)_m(MoO_3)_n$ precursors with different contents of MoO_3. As shown in the XRD patterns of various precursors with increasing temperature from RT to 1200 °C in Fig. S8 in the ESM, the initial components of the precursor were amorphous SiO_2, AlOOH, and $(NH_4)_6Mo_7O_{24}{\cdot}4H_2O$. The TG curves of the three precursors with different $m : n$ ratios were divided into four stages, as shown in Figs. 4(a)–4(c). The first stage occurred below 200 °C, with a mass loss of approximately 2.4% in the TG curves. Combined with the absorption peaks at 100 °C ($m : n = 9 : 1$), 92 °C ($m : n = 8 : 2$), and 112 °C ($m : n = 7 : 3$), it was concluded that the mass loss was due to the loss of bound water from $(NH_4)_6Mo_7O_{24}{\cdot}4H_2O$. The second stage mainly occurred in the range of 200–500 °C, and the absorption peaks were located at 445 °C ($m : n = 9 : 1$), 446 °C ($m : n = 8 : 2$), and 462 °C ($m : n = 7 : 3$), respectively. The maximum quality loss in this stage was due to the decomposition of AlOOH and $(NH_4)_6Mo_7O_{24}$. They completely decomposed at 500 °C, making 500 °C a standard boundary. The third stage occurred above 500 °C, but the temperature ranges corresponding to the three precursors were different, with "500–1110 °C" for $m : n = 9 : 1$, "500–934 °C" for $m : n = 8 : 2$, and "500–842 °C" for $m : n = 7 : 3$, which was related to the formation and decomposition of $Al_2(MoO_4)_3$. When the temperature was above 500 °C, MoO_3 reacted with Al_2O_3 to form $Al_2(MoO_4)_3$, which could reduce the volatilization of MoO_3. Therefore, the mass loss of the three precursors in this stage was very small, at 1.45%, 1.46%, and 1.47%, respectively. The formation of $Al_2(MoO_4)_3$ is endothermic reaction. However, there is no obvious absorption peak on the DSC curve, only a downward trend in the DSC curves. This should be related to the testing rate being too fast and the reaction being relatively slow. Interestingly, the stability of the three $Al_2(MoO_4)_3$ precursors was different. Its stability decreased with increasing MoO_3 content. The exothermic peaks at 970 °C ($m : n = 9 : 1$), 928 °C ($m : n = 8 : 2$), and 838 °C ($m : n = 7 : 3$) corresponded to their respective decomposition temperatures.

In fact, the decomposition of $Al_2(MoO_4)_3$ was more conducive to the growth of mullite whiskers because Al_2O_3 produced by the decomposition of $Al_2(MoO_4)_3$ was fine and highly reactive, and MoO_3 was directly melted to form a reaction molten pool. Therefore, stable $Al_2(MoO_4)_3$ was not conducive to the growth of mullite whiskers, which was also why the precursor with $m : n = 9 : 1$ did not grow whiskers at 1100 °C. The decomposed MoO_3 served as the molten phase for catalyzing whisker growth, which corresponded to the fourth stage reaction. The DSC curve sharply decreased in the fourth stage, which was caused by the large amount of heat absorbed during the synthesis of mullite. The testing speed was too fast, and no endothermic peak was formed. On the other hand, MoO_3 gradually evaporated in the fourth stage, causing the fourth mass loss.

In addition, to evaluate the thermal stability of porous ceramics, differential thermal analysis was also performed on $(3Al_2O_3{\cdot}1.8SiO_2)_9(MoO_3)_1$-1300 °C-3 h ceramics. As shown in Fig. 4(d), the weight loss of ceramics during the heating process was only 1.17%, and the DSC curve had no peak, indicating that the ceramics had good stability.

3.2 Mechanical properties

3.2.1 *Compressive strength*

Figure 5(a) shows the compressive strengths of various ceramics after sintering at 1300 °C, with sintering time ranging from 1 to 3 h. In particular, $(xAl_2O_3{\cdot}ySiO_2)_9(MoO_3)_1$ and $(xAl_2O_3{\cdot}ySiO_2)_8(MoO_3)_2$ ceramics exhibited notably superior compressive strengths. For $(3Al_2O_3{\cdot}1.8SiO_2)_9(MoO_3)_1$ ceramics, the compressive strength significantly increased with prolonged sintering time, rising from 1.49 MPa (1 h) to 4.81 MPa (3 h). However, after 3 h of sintering, the compressive strength of $(xAl_2O_3{\cdot}ySiO_2)_9(MoO_3)_1$ decreased with decreasing molar ratio of Al_2O_3 to SiO_2, decreasing from 4.81 MPa ($x : y = 3 : 1.8$) to 0.62 MPa ($x : y = 3 : 2.2$). Although the close arrangement of $x : y = 3 : 2.2$ ceramics could provide some strength, their load-bearing capacity under pressure was relatively weak because of the uniform smaller size of the whiskers. For $(3Al_2O_3{\cdot}1.8SiO_2)_m(MoO_3)_n$ ceramics, the compressive strength first

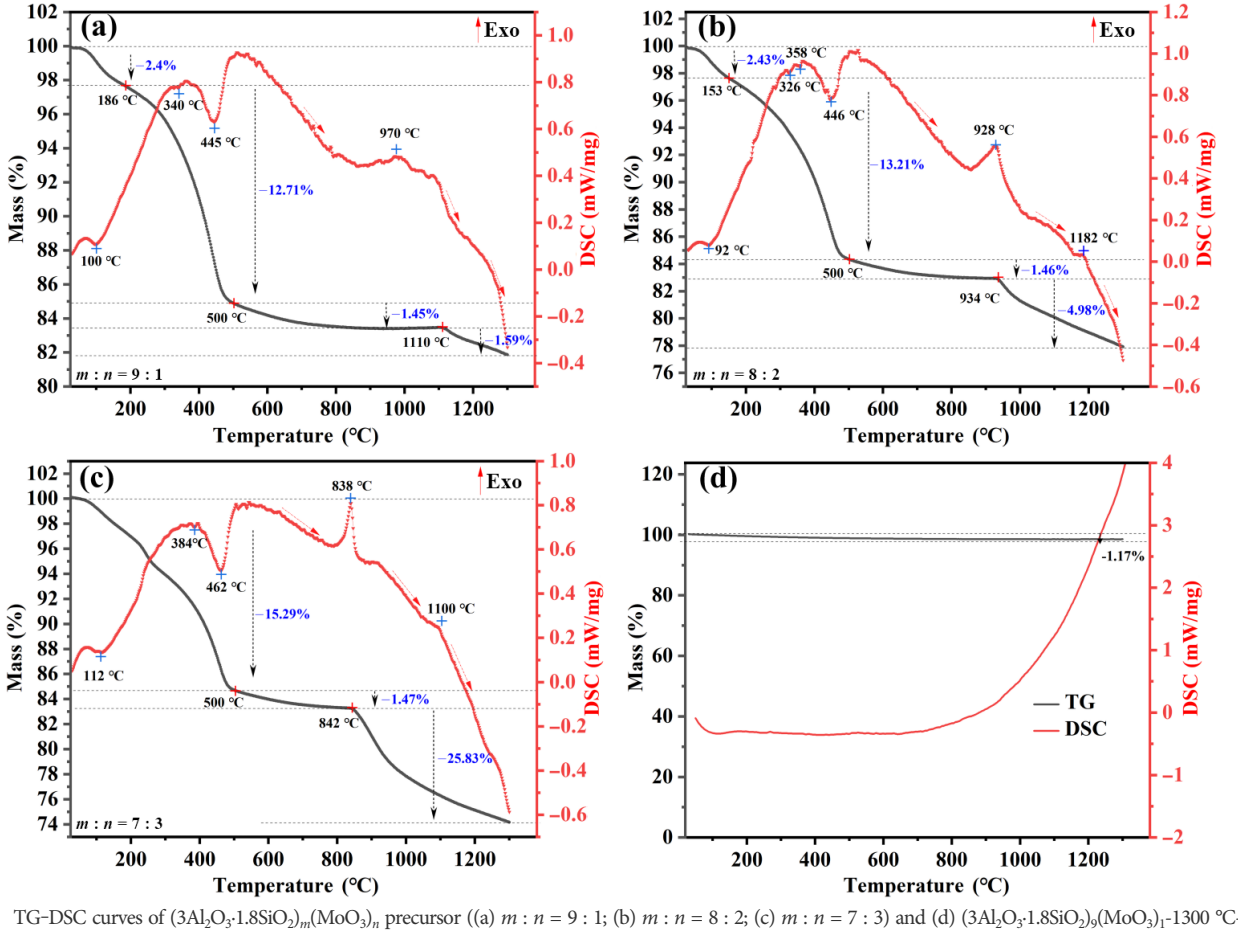

Fig. 4 TG-DSC curves of $(3Al_2O_3{\cdot}1.8SiO_2)_m(MoO_3)_n$ precursor ((a) $m : n = 9 : 1$; (b) $m : n = 8 : 2$; (c) $m : n = 7 : 3$) and (d) $(3Al_2O_3{\cdot}1.8SiO_2)_9(MoO_3)_1$-1300 °C-3 h ceramics.

increased and then decreased with increasing MoO_3 content, reaching a peak at a ratio of $m : n = 9 : 1$. At $m : n = 8 : 2$, when these whiskers were clustered together, the interconnection points lacked sufficient adhesion, resulting in lower overall strength. At $m : n = 10 : 0$, the lack of whiskers for construction and support significantly reduced the overall strength and stability of the structure, which macroscopically appears brittle.

Overall, $(3Al_2O_3{\cdot}1.8SiO_2)_9(MoO_3)_1$-1300 °C-3 h ceramics showed the best compressive strength. To evaluate its service effectiveness, a thermal shock test was performed on $(3Al_2O_3{\cdot}1.8SiO_2)_9(MoO_3)_1$-1300 °C-3 h ceramics. Figure S9 in the ESM illustrates the relationship between the compressive strength and number of thermal shock cycles between room temperature and 1300 °C. The ability of the porous ceramics to withstand thermal shock initially increased and then decreased as the number of cycles increased. The compressive strength of the ceramics increased by approximately 8.7% after 50 cycles and then decreased to 3.71 MPa after 100 cycles. Over this period, the overall strength retention rate was 77.13%, indicating a favorable level of thermal shock resistance.

The excellent mechanical performance of $(3Al_2O_3{\cdot}1.8SiO_2)_9(MoO_3)_1$-1300°C-3 h ceramics was attributed to their particular microstructure. The mullite whiskers inside most ceramics were relatively uniform in length, while the whiskers inside these ceramics were a mixture of multiple sizes. As observed in Fig. 2, the tiny and large whiskers created a multi-level reinforcement system that interlocked and supported each other. The tiny whiskers filled the gaps between the larger whiskers, increasing the density of the structure and reducing potential weak points. The distribution and structure of whiskers provided sufficient mechanical strength. They allowed for better adaptation and dispersion of external stresses by increasing the crack deflection area and improving the crack deflection resistance. By maintaining strength, the material also exhibits some degree of toughness, thus enhancing the overall performance of the ceramics. The mechanical properties of other ceramics were also related to their structure. The relationships among the preparation conditions, structure, and properties are discussed in detail in Section 3.6.

Analysis of Fig. 5(b) shows that within the margin of error, the minimum content of MoO_3 exhibited a higher density than the other contents. Since the alumina mold volume was fixed and the mass of the precursor powder added was consistent, there were no significant differences in mass loss during the heating process. Therefore, density was positively correlated with volumetric shrinkage. The increased concentration of MoO_3 as a flux caused the volumetric shrinkage rate of the sintered ceramics to gradually decrease, with the density falling from 1.32 to 0.64 g/cm^3. This change might be related to the development of mullite whisker structures and the increase in internal porosity [44]. The corresponding volume changes are presented in Fig. S10 in the ESM.

Figure 5(c) shows the specific strength of the ceramics sintered at 1300 °C. Under the sintering conditions of 1300 °C for 3 h, $(3Al_2O_3{\cdot}1.8SiO_2)_9(MoO_3)_1$ ceramics achieved a compressive strength of up to 4.81 MPa while maintaining a relatively low density of 0.76 g/cm^3, which helped reduce the overall structural load, resulting in a specific strength of 6328.9 (N·m)/kg. Tiny whiskers interspersed among the larger ones, and this more balanced distribution and structure provided sufficient strength

while allowing for better stress handling in different directions. Furthermore, the compressive strengths of $(3Al_2O_3{\cdot}1.8SiO_2)_9(MoO_3)_1$-1300 °C-3 h ceramics (which is named Sam-1 in Table 2) and recently reported porous ceramics (not limited to mullite ceramics) were compared, and the results are shown in Fig. 6.

Compared with the reported porous silica/mullite ceramics, highly porous YSZ ceramics, porous Y_2SiO_5 ceramics, etc. [45,56], Sam-1 ceramics prepared in this work exhibited excellent compressive strength and a lower density. Its specific strength stands out among similar mullite ceramics, reaching a high level. Although Yuan *et al.* [57] prepared mullite-bonded porous fiber mullite ceramics via gel casting, achieving a strength of 7.6 MPa

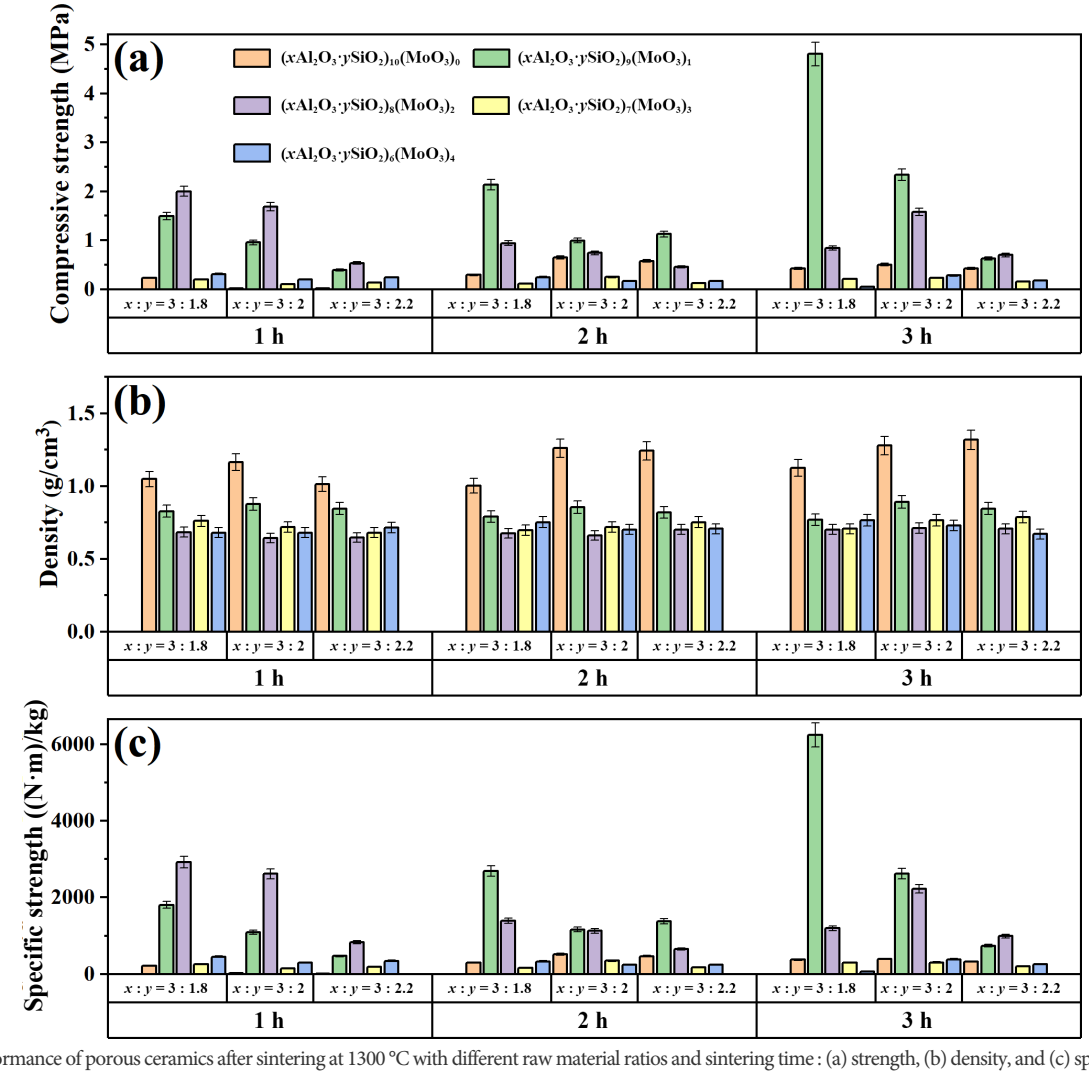

Fig. 5 Performance of porous ceramics after sintering at 1300 °C with different raw material ratios and sintering time : (a) strength, (b) density, and (c) specific strength.

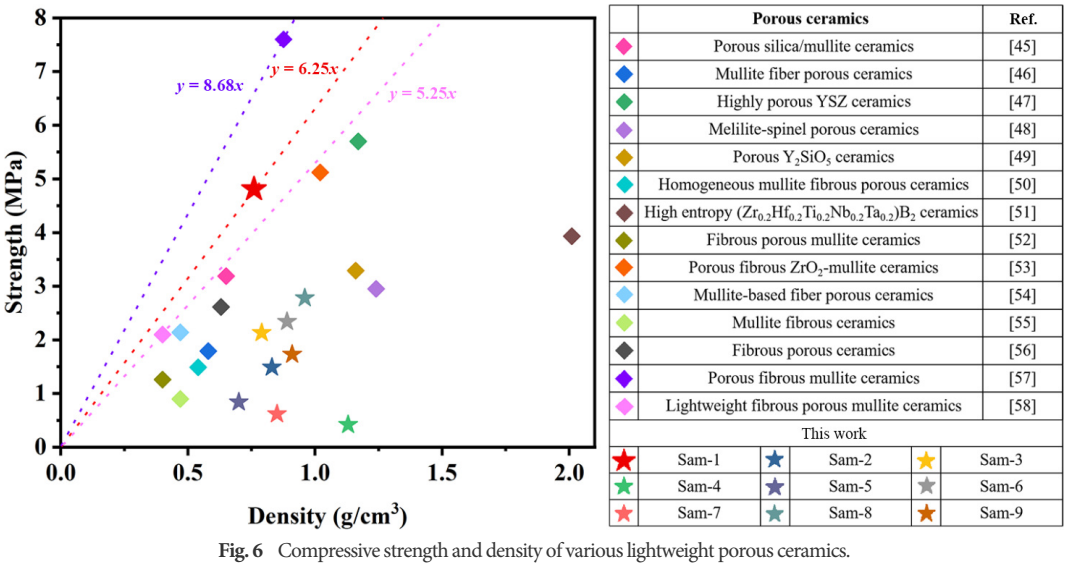

	Porous ceramics	Ref.
◆	Porous silica/mullite ceramics	[45]
◆	Mullite fiber porous ceramics	[46]
◆	Highly porous YSZ ceramics	[47]
◆	Melilite-spinel porous ceramics	[48]
◆	Porous Y_2SiO_5 ceramics	[49]
◆	Homogeneous mullite fibrous porous ceramics	[50]
◆	High entropy $(Zr_{0.2}Hf_{0.2}Ti_{0.2}Nb_{0.2}Ta_{0.2})B_2$ ceramics	[51]
◆	Fibrous porous mullite ceramics	[52]
◆	Porous fibrous ZrO_2-mullite ceramics	[53]
◆	Mullite-based fiber porous ceramics	[54]
◆	Mullite fibrous ceramics	[55]
◆	Fibrous porous ceramics	[56]
◆	Porous fibrous mullite ceramics	[57]
◆	Lightweight fibrous porous mullite ceramics	[58]
This work		
★ Sam-1	★ Sam-2	★ Sam-3
★ Sam-4	★ Sam-5	★ Sam-6
★ Sam-7	★ Sam-8	★ Sam-9

Fig. 6 Compressive strength and density of various lightweight porous ceramics.

清華大学出版社 Tsinghua University Press | SciOpen

and a density of 0.876 g/cm^3, this method relied on the curing of a suspension of ceramic powders with polymerized organic monomers. It must be performed under nitrogen protection to avoid interference from oxygen during the gel casting process. The preparation conditions were not only complex but also highly stringent in terms of environmental requirements. Similarly, Zhang *et al.* [58] used vacuum extrusion to fabricate a novel fibrous porous mullite network, achieving a low density of 0.40 g/cm^3, but the sintering process at lower temperatures (600 °C or below) required precise control of the removal of liquid B_2O_3 to ensure mechanical stability at high temperatures, making the preparation process equally intricate and requiring meticulous operation.

In contrast, Sam-1 ($(3Al_2O_3{\cdot}1.8SiO_2)_9(MoO_3)_1$-1300 °C-3 h) ceramics prepared in this work demonstrated superior compressive specific strength, leading among all similar ceramics. Its preparation process was simple and easy to perform, requiring no complex protective gas environment or precise removal processes. This method significantly outperforms the complex preparation procedures of other high-specific-strength ceramics.

To explore the relationship between the performance of porous ceramics and their preparation conditions, a sample with the best specific strength of porous ceramics produced at 1300 °C for 3 h with a composition of $3Al_2O_3{\cdot}1.8SiO_2)_9(MoO_3)_1$ was used as the benchmark and was named Sam-1. On this basis, the research scope was further expanded to include samples with varying sintering time (Sam-2 and Sam-3), different MoO_3 contents (Sam-4 and Sam-5), different molar ratios of Al_2O_3 to SiO_2 (Sam-6 and Sam-7), and different sintering temperatures (Sam-8 and Sam-9), as shown in Table 2. By comparing the structures and properties of these samples, the aim was to reveal the specific impacts of preparation parameters on the microstructure and macroscopic performance of the porous ceramics, thereby understanding the inherent patterns in material performance changes.

3.2.2 *Compressive rebound performance*

The compression rebound curves of the ceramics with different molar ratios of Al_2O_3 to SiO_2 (x : y) are shown in Fig. 7(a). At a strain of 0.5%, the maximum stress for x : y = 3 : 1.8 was close to that of x : y = 3 : 2. When the pressure was released, x : y = 3 : 1.8 resulted in approximately 0.1% more deformation than x : y = 3 : 2. The compressive stress decreased as the molar ratio of Al_2O_3 to SiO_2 increased. The loading curve for x : y = 3 : 2.2 exhibited a distinct plastic behavior, which was divided into elastic and yield stages. Starting from the elastic stage (0–0.12%), the slope of the compression curve remained almost constant, with the main load-bearing capacity provided by the three-dimensional framework structure of ceramics. The whisker-constructed supporting framework bent elastically, dispersed, and transferred an external force throughout the sample, maintaining the overall structure of the ceramic without collapsing [59]. In the yield stage (0.12%–0.5%), the slope of the loading curve was almost zero, with the whiskers gradually compacted and the structure beginning to collapse, forming small internal cracks that progressively extended outward. x : y = 3 : 2.2 was identified as a plastic material.

Figure 7(b) displays the compression rebound curves of ceramics with different MoO_3 addition amounts (m : n). The sample with m : n = 10 : 0 exhibited a higher maximum stress than that with m : n = 9 : 1. When the pressure was released, the rebound rates for m : n = 10 : 0 and m : n = 9 : 1 were essentially the same, while the loading curve for m : n = 8 : 2 demonstrated plastic characteristics. Figure 7(c) presents the stress–strain curves of the ceramics sintered for different durations, and the samples

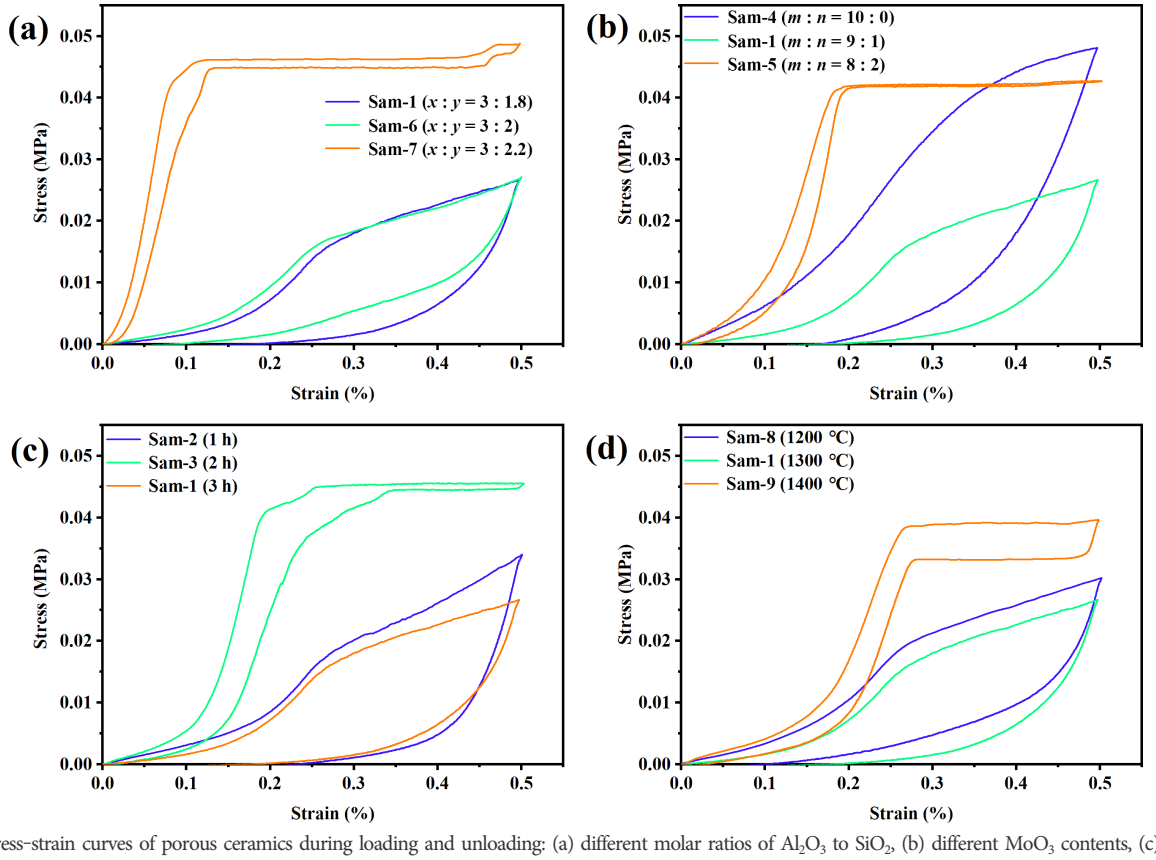

Fig. 7 Stress–strain curves of porous ceramics during loading and unloading: (a) different molar ratios of Al_2O_3 to SiO_2, (b) different MoO_3 contents, (c) different sintering time, and (d) different sintering temperatures.

sintered for 2 h exhibited significant plasticity. The samples sintered for 1 h achieved higher maximum stress and compressive rebound rates than those sintered for 3 h. Figure 7(d) shows the compressive rebound curves for the ceramics sintered at various temperatures, revealing that the samples sintered at 1400 °C exhibited plastic material properties. The Sam-1 ceramics, which were optimal for elasticity and plasticity, were selected to verify flexibility, as shown in Fig. 8.

Figure 8(a) shows the compression rebound performance of Sam-1 under different compressive strains. As the compressive strain increased, the retained deformation of Sam-1 decreased. At a strain of 0.75%, the sample nearly rebounded to its original dimensions upon pressure release. As the compressive strain increased, the microscopic pores of the sample compressed, leading to tighter locking of the whisker framework and an increase in elastic deformation, which resulted in a higher rebound rate. When the whisker framework compacted and the ceramic's ability to withstand external forces reached a critical state, internal cracks appeared, causing the loss of compression elastic performance. The fatigue resistance of Sam-1 at 0.5% strain is shown in Fig. 8(b). As the number of cycles increased, the supporting framework gradually transitioned from elastic deformation to plastic deformation after repeated loading, and the load-bearing structure got damaged with a certain degree of stress attenuation. After 30 cycles of fatigue testing, Sam-1 nearly returned to its original dimensions, maintaining approximately 99% of its elasticity. These results indicated that the elastic performance of porous ceramics existed only under minor deformations and exhibited good fatigue resistance.

3.2.3 Microscopic morphology: Comparison between original state, compressed state, and fractured state

As shown in the sample preparation flowchart in Fig. 9(a), type-1 samples (Figs. 9(b), 9(e), and 9(h)) were taken from the porous ceramics that had not undergone compression treatment. A small piece was precisely cut from this ceramic block before conducting mechanical performance tests to maintain its original structure and characteristics. This sample presented the original condition of the material in a stress-free state. Type-2 ceramic blocks (Figs. 9(c), 9(f), and 9(i)) were cut from the porous insulating ceramics after 30 cycles of fatigue testing. This sample underwent specific cyclic loading tests to simulate the repeated stress conditions encountered in practical applications. This represented the microstructural changes and damage accumulation of the material after experiencing fatigue loading. Type-3 (Figs. 9(d), 9(g), and 9(j)) was a fractured ceramic sample obtained after measuring the compressive strength through compression testing. This sample provided insights into the material's failure modes and fracture toughness.

As illustrated in Figs. 9(b), 9(e), and 9(h), the surface SEM images indicated that the whiskers grew well with moderate size and interlocked. Initially, the material possessed an ideal microstructure with a certain strength and orientation. After 30 cycles of fatigue testing, as shown in Figs. 9(c), 9(f), and 9(i), the gaps between the whiskers decreased. The sample experienced a certain degree of deformation during the fatigue process, with whiskers forming tighter bonds through interactions and adjustments, thereby better resisting the repeated fatigue stresses.

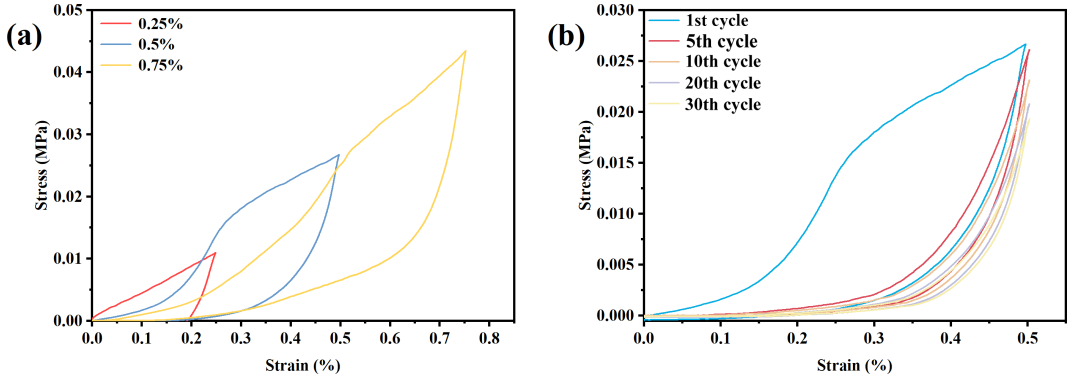

Fig. 8 (a) Compression elastic performance of Sam-1 under different compressive strains; (b) compression elastic performance of Sam-1 after 30 cycles at 0.5% strain.

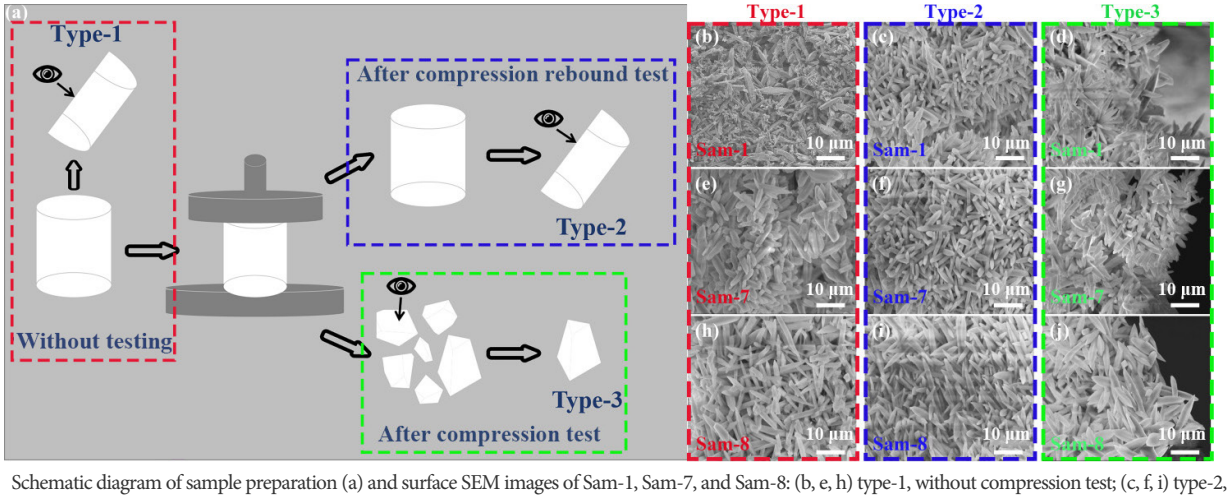

Fig. 9 Schematic diagram of sample preparation (a) and surface SEM images of Sam-1, Sam-7, and Sam-8: (b, e, h) type-1, without compression test; (c, f, i) type-2, after compression rebound test; (d, g, j) after compression test.

As shown in Figs. 9(d), 9(g), and 9(j), although the samples had fractured, the whiskers did not fracture, indicating high toughness and tensile strength [60]. The bonding between whiskers unraveled on the fracture surface, and the failure of the sample primarily occurred at the connections between the whiskers rather than within the whiskers themselves.

3.3 Thermal properties

3.3.1 *Thermal conductivity*

The thermal conductivities of different types of insulating ceramics are displayed in Table 3 [51,57,61–64]. Sam-1 had a thermal conductivity of 0.260 W/(m·K), which was the lowest among all the samples. Compared with those of $(Zr_{0.2}Hf_{0.2}Ti_{0.2}Nb_{0.2}Ta_{0.2})B_2$ ceramics, alumina whisker foam ceramics, and ZrO_2-mullite porous ceramics, the thermal conductivity of Sam-1 was approximately 49.02%, 70.08%, and 81.02% lower, respectively. Moreover, mullite–SiC foam ceramics, porous nanostructured mullite ceramics, and porous fibrous mullite ceramics had thermal conductivities approximately 5.77%, 515.38%, and 45.38% higher than that of Sam-1, respectively. Therefore, under the same conditions, Sam-1 had the lowest thermal conductivity. Based on the thermal conductivity and density of the material, this ceramic sample was found to be more suitable for applications requiring lightweight and efficient thermal insulation.

3.3.2 *Thermal insulation performance*

The thermal insulation performance of porous insulating ceramics formed under different conditions was studied. Before the experiment, insulating cotton with dimensions of 150 mm × 150 mm was properly trimmed to create a moderate-sized opening. Subsequently, the sample to be tested was embedded within it. The insulating properties of the cotton effectively blocked the direct heating of the ceramic's backside by the butane flame, ensuring the accuracy and reliability of the test results of thermal insulation performance. The experimental process during the thermal insulation performance test is presented in Fig. S11 in the ESM. The test results are shown in Fig. S12 in the ESM.

The maximum backside temperature of the ceramics under a 1300 °C butane flame impact was concentrated between 190 and 350 °C, indicating long-lasting durability. Among them, the backside temperatures of Sam-1, Sam-5, and Sam-8 remained below 200 °C, indicating excellent thermal insulation performance. The curves could be divided into two stages based on time : 0–400 and 400–1700 s. In the first stage, the ceramics' backside temperature rapidly increased to its peak as it began to contact the flame. Sample Sam-4 reached the highest backside temperature of 348.67 °C, while the peak backside temperatures of the ceramics varied depending on the firing conditions and precursor types. Sam-1 exhibited the lowest peak backside temperature among all the samples, at only 192.89 °C, which was 44.68% lower than that of Sam-4. In the second stage, the heat transfer rate within the ceramics was equal to the heat dissipation rate, resulting in a stable heat distribution. Consequently, the rise in temperature slowed down and ultimately stabilized. To further explore the effects of different firing conditions and precursor types on the thermal insulation performance of porous insulating ceramics, we compared the temperature variation curves of the backsides of different types of ceramics by controlling variables, as shown in Fig. 10.

Figure 10(a) compares the thermal insulation performance of ceramics with different molar ratios of Al_2O_3 to SiO_2. As the molar ratio of Al_2O_3 to SiO_2 decreased, the peak backside temperature of the ceramics continuously rose. Sam-7 ($x : y = 3 : 2.2$) had a relatively dense structure, with more extensive contact between the solid components, making heat transfer easier. Sam-6 ($x : y = 3 : 2$) had a smaller specific surface area and larger pore sizes, and the air in the pores could more easily form convection. In Sam-1 ($x : y = 3 : 1.8$), the presence of whiskers and pores of varying sizes created a non-uniform structure with the highest porosity (74.18%) that helped reduce the overall heat transfer, allowing the backside temperature of the ceramic to be controlled at 180.08 °C, which was 31.69% lower than that of Sam-7 ($x : y = 3 : 2.2$).

Figure 10(b) shows the differences in the thermal insulation performance of the ceramics with varying contents of MoO_3. Sam-1 ($m : n = 9 : 1$) and Sam-5 ($m : n = 8 : 2$) featured a fully whisker-constructed structure, while Sam-4 ($m : n = 10 : 0$) was a blocky material with hardly any whisker formation. The three-dimensional network structure formed by whiskers increased the specific surface area and microscopic voids of the ceramics, facilitating air capture and heat dissipation. As a result, the backside temperatures of Sam-1 ($m : n = 9 : 1$) and Sam-5 ($m : n = 8 : 2$) were approximately 48.95% lower than that of Sam-4 ($m : n = 10 : 0$).

The backside temperatures of porous ceramics with different sintering time are shown in Fig. 10(c). The backside temperature of the ceramics decreased with increasing sintering time. The backside temperature of Sam-1 (3 h) was 39.36% lower than that of Sam-2 (1 h). Figure 10(d) shows the thermal insulation performance of the ceramics at different sintering temperatures. Sam-9 (1400 °C) showed the highest peak backside temperature, which was 37.53% higher than that of Sam-1 (1300 °C). Sam-1 (1300 °C) maintained a backside temperature below 200 °C after exposure to 1300 °C for 1700 s.

3.3.3 *Infrared thermal imaging*

To simulate the ceramics' operating environment further, a butane flame was continuously applied to the front surface of the Sam-1 sample, and infrared thermal imaging technology was used to monitor the temperature changes on its back side. The experimental setup is shown in Fig. S13 in the ESM.

Figure 11(a) shows that during the 10-min continuous heating process, the ambient temperature rapidly increased to 538.7 °C,

Table 3 Thermal properties of different types of insulating ceramics

Sample	Density (g/cm³)	Thermal conductivity (W/(m·K))	Ref.
Sam-1	0.76	0.260	This work
$(Zr_{0.2}Hf_{0.2}Ti_{0.2}Nb_{0.2}Ta_{0.2})B_2$ ceramics	2.01	0.510	[51]
Alumina whisker foam ceramics	0.65	1.370	[61]
ZrO_2–mullite porous ceramics	1.65	0.869	[62]
Mullite–SiC foam ceramics	0.79	0.275	[63]
Porous nano-structured mullite ceramics	2.10	1.600	[64]
Porous fibrous mullite ceramics	0.88	0.378	[57]

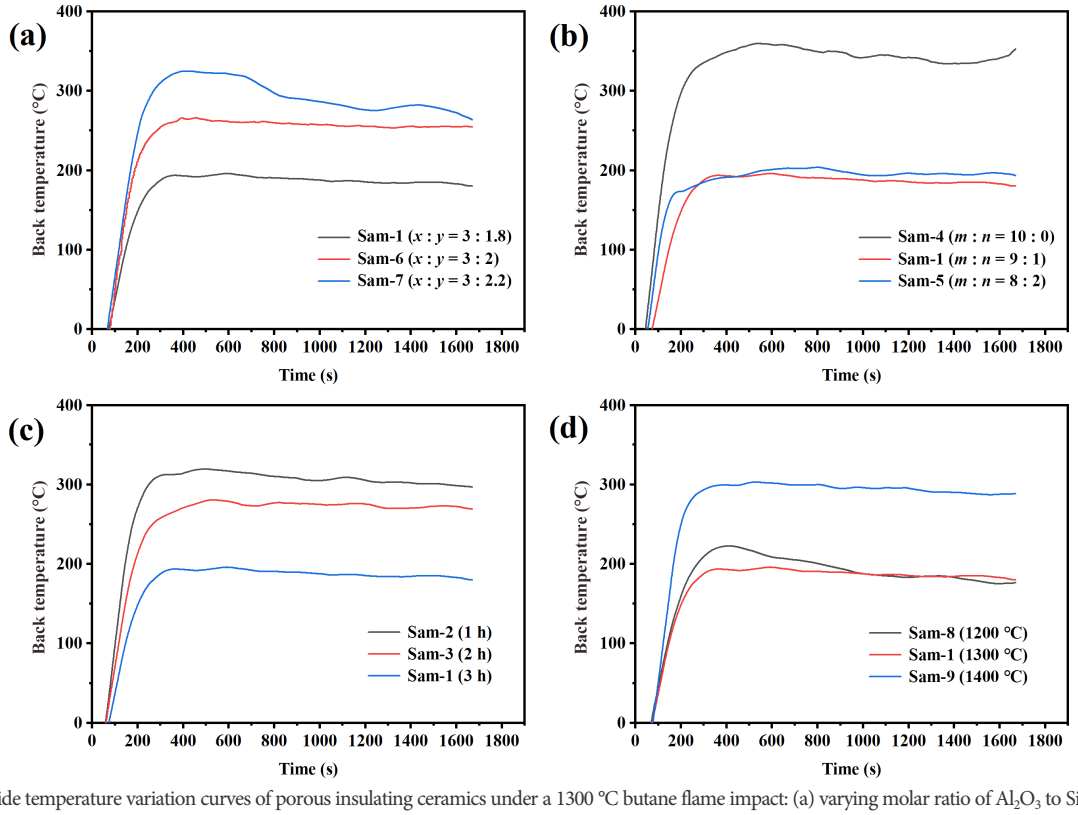

Fig. 10 Backside temperature variation curves of porous insulating ceramics under a 1300 °C butane flame impact: (a) varying molar ratio of Al_2O_3 to SiO_2, (b) varying MoO_3 content, (c) varying sintering time, and (d) varying sintering temperature.

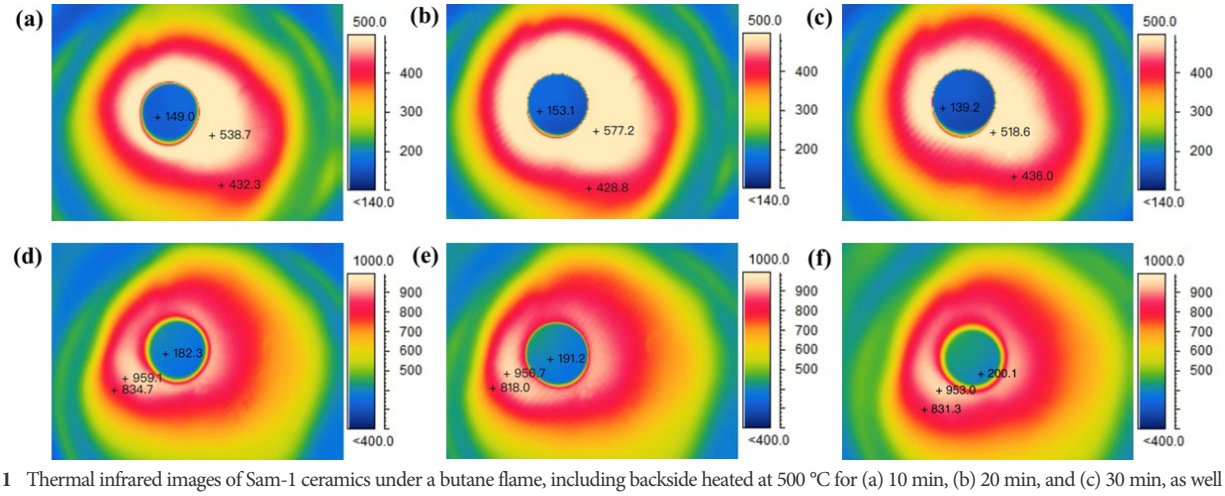

Fig. 11 Thermal infrared images of Sam-1 ceramics under a butane flame, including backside heated at 500 °C for (a) 10 min, (b) 20 min, and (c) 30 min, as well as the backside heated at 1000 °C for (d) 10 min, (e) 20 min, and (f) 30 min.

and the temperature on the back side of the sample reached 149.0 °C because of the heat conduction effect. As the heating time increased, the backside temperature gradually stabilized at approximately 145 °C, as shown in Figs. 11(b) and 11(c), with the temperature difference between the center of the backside and the ambient temperature maintaining stable at 400 °C. Furthermore, when the ambient temperature was increased to 1000 °C and re-heating for 10 min, as shown in Fig. 11(d), the temperature on the back side of the sample increased to 182.3 °C. With prolonged heating, the temperature eventually stabilized at approximately 200 °C, as recorded in Figs. 11(e) and 11(f), with the temperature difference reaching 800 °C. The experimental results indicate that the porous ceramics possessed excellent thermal insulation performance, which is consistent with previous experimental findings, which showed that they could maintain a lower backside temperature in extremely high-temperature environments, thus effectively protecting the structural integrity and functionality.

3.3.4 *Thermal expansion*

During the heat treatment process from room temperature to 1000 °C, the thermal expansion coefficients of the porous ceramics initially tended to increase but then stabilized as the temperature increased, ranging from 4×10^{-6} to 6×10^{-6} K^{-1}. In the range of room temperature–300 °C, the thermal vibrations of atoms cause lattice deformation and overall expansion [65]. When the test temperature exceeded 330 °C, the crystal structure gradually approached a balanced state, and the thermal expansion coefficient tended to flatten out. The effects of different molar ratios of Al_2O_3 to SiO_2 on the thermal expansion coefficient of the ceramics are shown in Fig. 12(a). The structure of Sam-7 ($x : y =$

3 : 2.2) was dense with smaller pores, leading to a higher thermal expansion coefficient, which decreased as the residual SiO_2 began to melt. As the molar ratio of Al_2O_3 to SiO_2 increased, the thermal expansion of Sam-1 (x : y = 3 : 1.8) did not descend and was very stable. As shown in Fig. 12(b), the increase in the MoO_3 content caused the peak thermal expansion coefficient of the ceramic samples to first decrease and then increase, with a peak difference of 1.4×10^{-6} K^{-1}. Figures 12(c) and 12(d) compare the variations in the thermal expansion coefficients with different sintering time and temperatures. The differences in the thermal expansion effects of the ceramics sintered at various time and temperatures were relatively small, with the thermal expansion coefficients differing by less than 0.65×10^{-6} K^{-1}.

3.4 Growth mechanism of mullite whiskers and formation mechanism of porous ceramics

Figure 13 shows the growth mechanism of mullite whiskers and formation mechanism of porous ceramics, and the detailed composition evolution of ceramic precursors with temperature is shown in Fig. S8 in the ESM. Without heat treatment, the ceramic body only contains AlO(OH), amorphous SiO_2, and $(NH_4)_6Mo_7O_{24}\cdot4H_2O$. When the temperature is above 200 °C, AlO(OH) and $(NH_4)_6Mo_7O_{24}$ gradually decompose into hexagonal γ-Al_2O_3 and MoO_3, mainly in the range of 200–500 °C, according to Eqs. (1) and (2). When the temperature exceeds 500 °C, MoO_3 and Al_2O_3 gradually react into $Al_2(MO_4)_3$ according

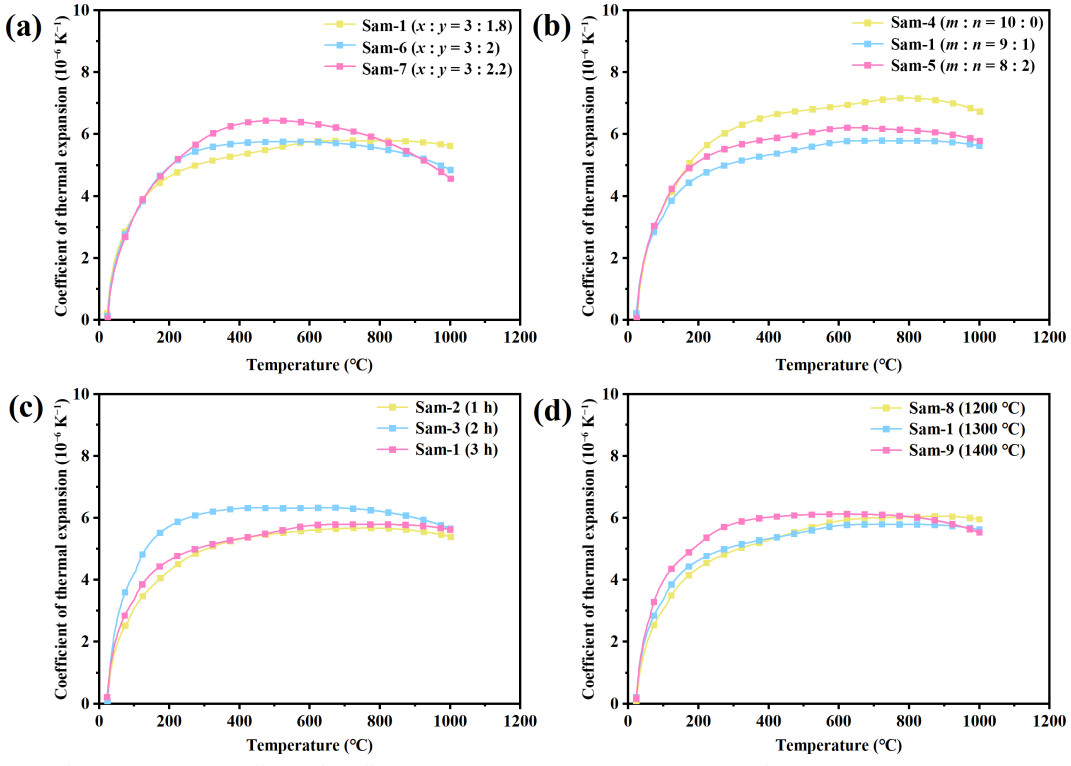

Fig. 12 Comparison of thermal expansion coefficients for different porous ceramics : (a) varying molar ratios of Al_2O_3 to SiO_2, (b) varying MoO_3 contents, (c) varying sintering time, and (d) varying sintering temperatures.

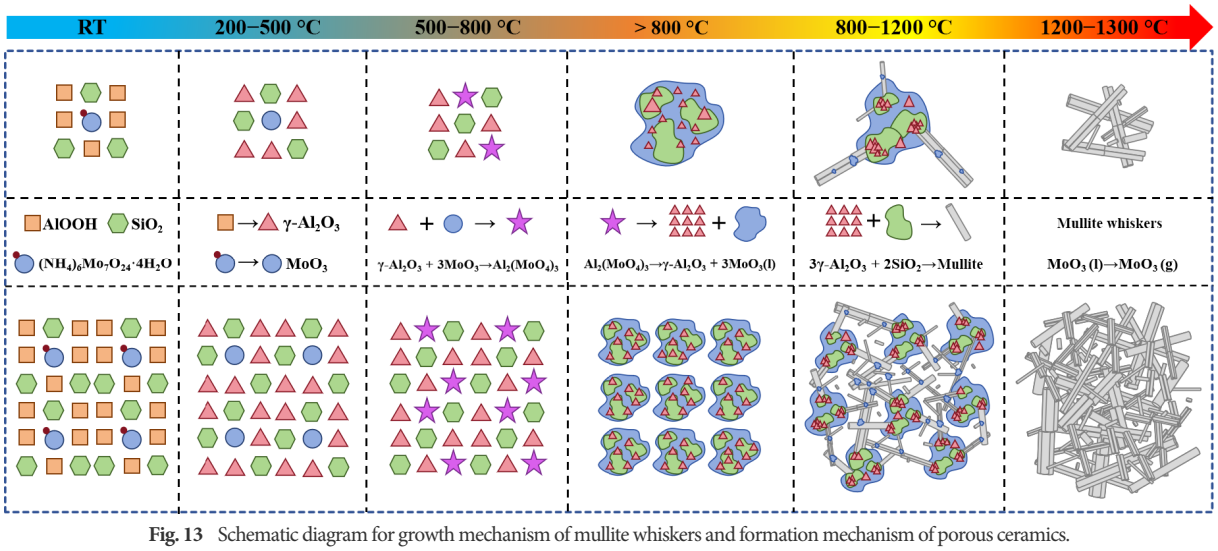

Fig. 13 Schematic diagram for growth mechanism of mullite whiskers and formation mechanism of porous ceramics.

to Eq. (3). The formation of $Al_2(MO_4)_3$ with a melting point of 795 °C can effectively improve the stability of MoO_3 and reduce its volatilization effect [42,66]. As shown in Fig. S8(d) in the ESM, $Al_2(MO_4)_3$ could still be identified at 800 °C. When the temperature is above 800 °C, $Al_2(MO_4)_3$ gradually decomposes into highly reactive fine Al_2O_3 and low-melting-point MoO_3 (Eq. (4)). MoO_3 forms a liquid phase rich in SiO_2, and the highly reactive fine Al_2O_3 readily dissolves in it, reacting with SiO_2 to form mullite based on Eq. (5). This reaction usually occurs at 800–1200 °C. The higher the content of MoO_3, the lower the temperature at which mullite is generated. In this work, mullite whiskers have already formed at 1000 °C in precursors of $m : n$ = 8 : 2 and $m : n$ = 7 : 3, while it takes 1200 °C to form whiskers in the precursor of $m : n$ = 9 : 1.

$$4AlO(OH)(s) \overset{>200\ ^\circ C}{\rightarrow} 2\gamma\text{-}Al_2O_3(s) + 2H_2O(g) \quad (1)$$

$$(NH_4)_6Mo_7O_{24} \cdot 4H_2O(s) \overset{>200\ ^\circ C}{\rightarrow} 6NH_3(g) + 7MoO_3(s) + 7H_2O(g) \quad (2)$$

$$\gamma\text{-}Al_2O_3(s) + 3MoO_3(s) \overset{>500\ ^\circ C}{\rightarrow} Al_2(MO_4)_3(s) \quad (3)$$

$$Al_2(MO_4)_3(s) \overset{>800\ ^\circ C}{\rightarrow} \gamma\text{-}Al_2O_3(s) + 3MoO_3(l) \quad (4)$$

$$3\gamma\text{-}Al_2O_3(s) + 2SiO_2(l) \xrightarrow{\text{In molten } MoO_3} \text{Mullite whikers}(s) \quad (5)$$

After MoO_3 in ceramic bodies is melted, many local melt pools are formed, and the molten salt in each melt pool catalyzes the growth of multiple mullite whiskers in different directions. The *in-situ* growth of whiskers causes the rearrangement of atoms in Al_2O_3 and SiO_2. The generation of whiskers changes the internal structure of ceramics, transforming the dense structure into a porous structure. The mullite whiskers grown in each melt pool approach each other and initially overlap through the liquid phase attached to the whiskers and further react and fuse to form stable whisker overlapped or interlocked joints. As the temperature increases, most of liquid-phase MoO_3 evaporates, and a porous structure consisting entirely of mullite whiskers is formally formed. The residual unreacted molten SiO_2 and Al_2O_3 further react to generate new whiskers or mullite phases at the overlapping position, improving the connection strength between the whiskers. The primary formation mechanism of the porous structure in this work involves atomic rearrangement during the growth of crystal whiskers by the reaction of Al_2O_3 and SiO_2 under the catalysis of MoO_3. In addition, the decomposition of $(NH_4)_6Mo_7O_{24}\cdot4H_2O$ and AlOOH and the volatilization of molten MoO_3 all contribute to the increase in porosity.

The generation mechanism of various porous ceramics in this work is consistent, but the preparation parameters significantly affect the structure and properties of the porous ceramics.

Figure 14 summarizes the effects of four preparation parameters on the structure and properties of porous ceramics. By adjusting the preparation parameters, the morphology and structure of whisker growth influence the mechanical properties and thermal insulation performance of porous thermal insulation ceramics. The mechanical properties are reflected by the compressive strength, density, and specific strength, while the thermal insulation performance is represented by the temperature

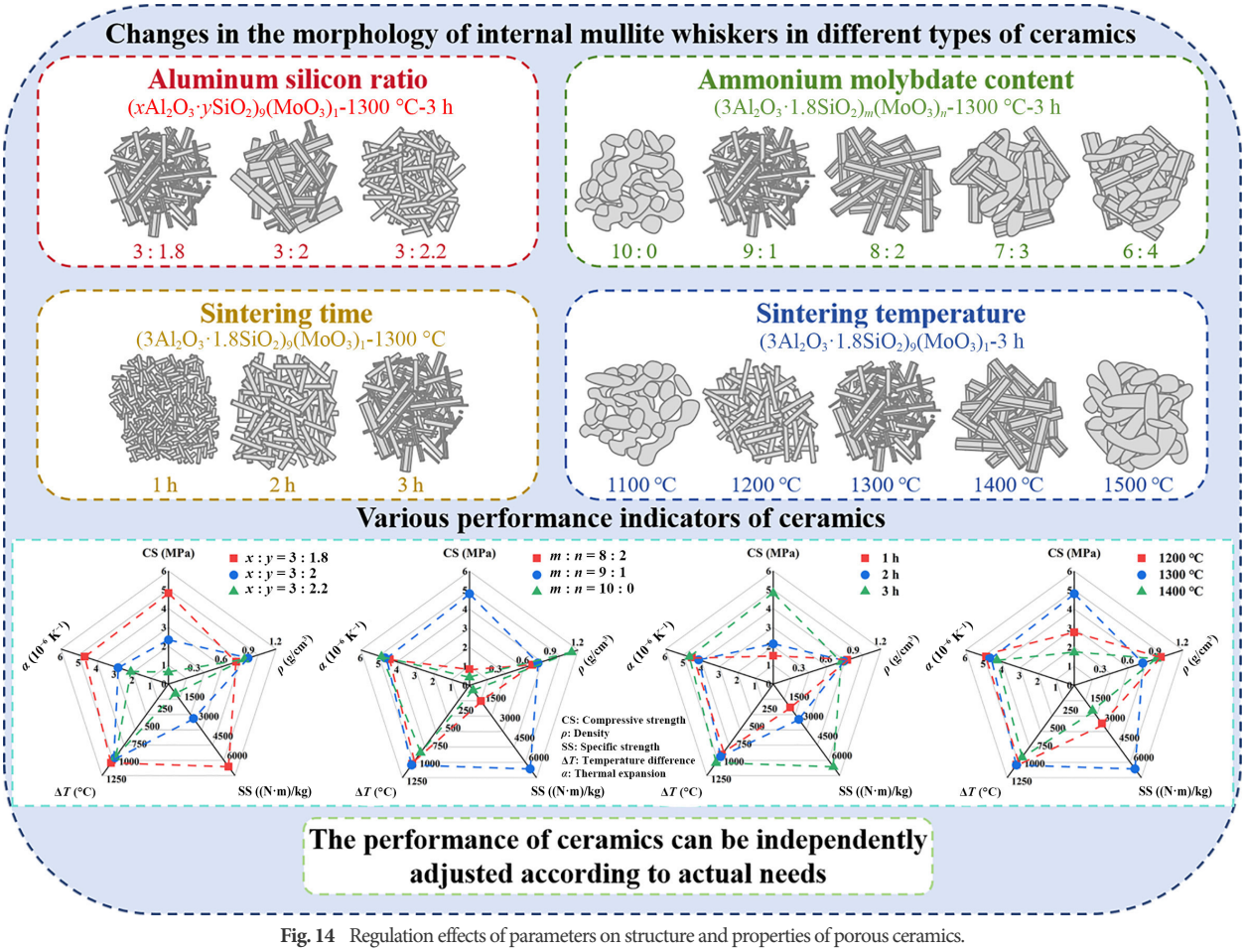

Fig. 14 Regulation effects of parameters on structure and properties of porous ceramics.

difference between the front and back surfaces of the ceramics after approximately 30 min of continuous impact under a butane flame at 1300 °C, as well as the thermal expansion coefficient.

(1) Influence of molar ratio of Al_2O_3 to SiO_2

For $(xAl_2O_3{\cdot}ySiO_2)_9(MoO_3)_1$-1300 °C-3 h, an increase in SiO_2 content promoted the generation of mullite, but the difference in the amount of mullite generated under these three ratios (x : y = 3 : 1.8, 3 : 2, and 3 : 2.2) was not significant. However, the x : y ratio significantly influences the morphology of mullite whiskers and the porous ceramic structure. Under three conditions, the whiskers of x : y = 3 : 2.2 are the smallest, and the size distribution is the most uniform. The whiskers of x : y = 3 : 2 are the largest, but their width is uneven. The size of the whiskers of x : y = 3 : 1.8 varies, and there is a distribution of mixed whiskers of different sizes. The structural differences significantly impact the mechanical properties and the insulation effect. For ceramics with x : y = 3 : 2.2, the whiskers are too small, and the overlapping structure is poor, which is similar to particle accumulation. The deflection effect of whiskers is inadequate, and the crack propagation is fast, resulting in easy structural damage. The cross-section of Fig. 9(g) is remarkably straight. Therefore, the compressive strength is only 0.62 MPa. The other two types of ceramics have longer crystal whiskers and significantly overlapping structures. The whisker deflection can be exerted during the loading process, resulting in good load-bearing capacity. Notably, in ceramics with x : y = 3 : 1.8, there is an interlaced distribution of tiny and large whiskers, which is more like a small whisker-reinforced large whisker skeleton. The tiny and large whiskers create a multi-level reinforcement system that interlocks and supports each other. First, this structure can increase the overlapping nodes of the whiskers, thereby increasing the crack deflection area and improving the bearing capacity. The fracture surface shown in Fig. 9(d) is layered and very tortuous. Second, tiny whiskers support large whiskers and increase their deflection resistance. When the force is too high, the combination of whiskers with different sizes can improve the deformation resistance, while when the force is too low, it can improve the rebound performance. Therefore, ceramics with x : y = 3 : 1.8 exhibit excellent mechanical properties.

Generally, the higher the porosity, the better the insulation effect. The ceramics with x : y = 3 : 1.8 have the highest porosity (74.18%) and the best insulation effect, which meets the above empirical viewpoint. However, the porosity of the ceramics with x : y = 3 : 2.2 (69.77%) is greater than that with x : y = 3 : 2 (66.22%), but the former's insulation effect is the worst, which is attributed to the short whisker accumulation structure. Although the ceramics with x : y = 3 : 2.2 have the highest specific surface area (2.08 m^2/g) and the lowest pore size (3.9 μm), the stacking form of the smallest whiskers increases the proportion of solid heat transfer per unit area. Although ceramics with x : y = 3 : 2 have a lower porosity, the whiskers overlap, and the solid heat transfer area per unit area is still relatively small. Therefore, the overlapping structure of two sizes of whiskers inside the ceramics with x : y = 3 : 1.8 not only has substantial load-bearing capacity but also has high porosity.

(2) Influence of MoO_3 content

MoO_3 is the most commonly used flux for catalyzing mullite whiskers, but the added amount must be controlled. When the amount of MoO_3 added is high, excessive growth of whiskers will occur. The excessive growth of mullite whiskers in the ceramics with m : n = 7 : 3 and m : n = 6 : 4 is evident, with some whiskers growing into large grains, and the distribution of large grains and whiskers is very uneven. This uneven distribution can lead to stress concentration, accelerate crack propagation, and significantly reduce the mechanical properties. The compressive strengths of the ceramics with m : n = 7 : 3 and m : n = 6 : 4 are only 0.21 and 0.05 MPa, respectively. Therefore, they cannot be applied industrially. Moreover, excessive growth of mullite whiskers also reduces the porosity of these two ceramics to 37.73% and 34.46%, respectively. If MoO_3 is not added, the ceramic will not evolve into a porous structure. Therefore, the atomic rearrangement during the reaction between Al_2O_3 and SiO_2 catalyzed by MoO_3 is the primary formation mechanism of porous ceramics.

Compared with those in the ceramics with m : n = 9 : 1, the mullite whiskers in the ceramics with m : n = 8 : 2 present a perfectly round needle-like structure, with no structural defects and a uniform size. However, these whiskers are independent of each other, have poor adhesion, and appear very loose. This structure results in poor mechanical properties of ceramics, with a compressive strength of less than 1 MPa. Grinding ceramics with m : n = 8 : 2 can obtain uniformly dispersed mullite whiskers. Therefore, the condition of m : n = 8 : 2 is more suitable for preparing whiskers. On the other hand, the porosities and densities of these two ceramics are very similar, and their insulation effects are not very different.

(3) Influences of sintering time and temperature

Extending time or increasing temperature is beneficial for the growth of mullite whiskers, but the efficiency of temperature in promoting growth is more substantial. When the sintering time was extended from 1 to 2 h, the whiskers grew from uniform 5.93 μm to uniform 14.67 μm. After 3 h of processing, a portion of whiskers adhered together to form large whiskers, resulting in the arrangement of whiskers of different sizes. As time passes, the ceramic structure evolves from tiny to multi-sized whisker overlapping, and the porosity gradually increases. Both the mechanical strength and insulation effects increase with time.

Excessive temperature can cause excessive growth of mullite whiskers, which is similar to the effect of excessive flux. Large grains are unevenly distributed in porous ceramics treated at temperatures not lower than 1400 °C, causing stress concentration and severe strength attenuation. When the temperature is too low, mullite whiskers cannot be generated, and the ceramic structure is not porous. The whiskers in ceramics treated at 1200 °C are similar to those treated at 1300 °C, but the difference in whisker size is still not significant. Therefore, the compressive strength of the former is lower. However, the ceramic treated at 1200 °C has the highest porosity, indicating excellent thermal insulation performance.

Finally, to clarify the advantages of the porous ceramics prepared in this work without using any pore-forming agents, the performance of $(3Al_2O_3{\cdot}1.8SiO_2)_9(MoO_3)_1$-1300 °C-3 h (Sam-1) ceramics is compared with that of porous mullite materials prepared by traditional pore-forming methods. The performance comparison is shown in Table 4. Compared with Refs. [67,72,74,75], without the addition of pore-forming agents, although there is a significant difference in compressive strength, the density and porosity of Sam-1 are superior. The porosity of 74.18% for Sam-1 is still greater than half that of the porous ceramics, and the strength is also considerable. This innovative process greatly simplifies the preparation process of porous ceramics, eliminates the use of foaming agents, and improves the controllability of component dimensions.

4 Conclusions

In this study, nanoalumina sol and nanosilica sol were used as raw materials, and ammonium molybdate tetrahydrate was employed

Table 4 Performance comparison between ceramics prepared in this work and ceramics prepared by traditional pore-foaming technology

Pore-forming agent	Compressive strength (MPa)	Density (g/cm^3)	Porosity (%)	Thermal conductivity (W/(m·K))	Ref.
H_2O_2 solution	1.72	—	83.52	—	[9]
Water-soluble epoxy resin of ethylene glycol diglycidyl ether, polyethyleneimine	4.4–7.6	—	61.1–71.7	0.378–0.467	[57]
MASHSs (magnesia-aluminum spinel hollow spheres)	22.43	1.25	64.6	0.368	[67]
Bioactive yeast cell	—	—	55	—	[68]
Lignin fiber	6.11	0.98	72.82	—	[69]
Starch	1.35–4.98	—	49.50–62.67	—	[70]
Rayon fibers	1.31–1.67	—	43.2–59.3	—	[71]
Rice husk ash	11.07	1.092	57.48	0.186	[72]
Sucrose, magnesium nitrate	1.15	—	93.46	—	[73]
Cenospheres (MA)	37.1	1.7	46	1.36	[74]
Graphite	—	1.97	36.4	—	[75]
Sodium lauryl sulfate	5.5	—	77.3	0.37–0.45 (1100 °C)	[76]
Cold water-insoluble starch	1.22	0.28–0.67	76.4–91.3	0.035–0.043	[77]
Sodium dodecyl sulfate (SDS)	6.23	—	80.71	—	[78]
—	4.81	0.76	74.18	0.260	This work (Sam-1)

as a flux. By controlling factors such as the molar ratio of Al_2O_3 to SiO_2 (x : y), ammonium molybdate content (m : n), sintering temperature (T), and sintering time (t), porous ceramics with excellent performance constructed entirely of mullite whiskers were successfully prepared. At x : y = 3 : 1.8, m : n = 9 : 1, T = 1300 °C, and t = 3 h, $(3Al_2O_3{\cdot}1.8SiO_2)_9(MoO_3)_1$-1300 °C-3 h ceramics exhibited a high compressive strength of 4.81 MPa and a low density of 0.76 g/cm^3. Their main components included mostly mullite and small amounts of SiO_2 and Al_2O_3. Microstructural analysis of $(3Al_2O_3{\cdot}1.8SiO_2)_9(MoO_3)_1$-1300 °C-3 h ceramics revealed that the interlocking of multi-size whiskers formed a multi-level reinforcement structure, providing the ceramics with good fatigue resistance under small deformations. After 100 thermal shock cycles between room temperature and 1300 °C, the compressive strength retention rate was 77.13%. In addition, the multi-scale whisker overlapping structure also has a high specific surface area (1.83 m^2/g), high porosity (74.18%), and small pore size (7.44 μm), showing an excellent thermal insulation effect. The thermal conductivity of the ceramic was measured to be 0.260 W/(m·K), which was much lower than that of many existing insulating materials. Insulation performance tests revealed that during a 1300 °C flame impact test, the back surface temperature of $(3Al_2O_3{\cdot}1.8SiO_2)_9(MoO_3)_1$-1300 °C-3 h ceramics remained below 200 °C. In addition, the thermal expansion coefficient of the ceramics was mainly in the range of 4×10^{-6} K^{-1} at 200 °C to 6×10^{-6} K^{-1} at 1000 °C, indicating good dimensional stability. Additionally, this study investigated the formation mechanism of porous ceramics and the regulatory mechanism between parameters, structure, and properties. Without the addition of any pore-forming agents, the formation of porous ceramics is derived from the *in-situ* growth of mullite whiskers in the molten MoO_3 reactive molten pools. Essentially, it was the atomic rearrangement of Al_2O_3 and SiO_2. The molar ratio of Al_2O_3 to SiO_2 had a significant effect on the morphology of crystal whiskers, while the flux and sintering conditions mainly affected the growth of crystal whiskers. A series of performance-adjustable porous ceramics can be obtained by adjusting four parameters.

Acknowledgements

This work was supported by the Fundamental Research Funds for the Central Universities of Civil Aviation University of China (No. 3122024050) and the Undergraduate Innovation Project of Civil Aviation University of China (Nos. 202410059049 and IECAUC2025043).

Availability of data and materials

The data that support the findings of this study are available fromthe corresponding author upon reasonable request.

Competing interests

The authors have no competing interests to declare that are relevant to the content of this article.

Electronic Supplementary Material

Supplementary material is available in the online version of this article at https://doi.org/10.26599/JAC.2025.9221055.

References

[1] Xu J, Shao YQ, Feng XY, *et al.* Low sintering shrinkage porous ceramics: Principles, progress, and perspectives. *J Adv Ceram* 2025, **14**: 9221015.

[2] Yang RW, Xu J, Guo J, *et al.* High wave transmittance and low thermal conductivity Y–α-SiAlON porous ceramics for high-temperature radome applications. *J Adv Ceram* 2023, **12**: 1273–1287.

[3] Hernández MF, Suárez G, Cipollone M, *et al.* Formation, microstructure and properties of aluminum borate ceramics obtained from alumina and boric acid. *Ceram Int* 2017, **43**: 2188–2195.

[4] Liu YY, Tian ZL, Zheng LY, *et al.* Synergistic promotion of dielectric and thermomechanical properties of porous Si_3N_4 ceramics by a dual-solvent template method. *J Adv Ceram* 2024, **13**: 1622–1634.

[5] Xiao YY, Liu SH, Zhou JL, *et al.* Lightweight, strong, and thermally insulating polybenzoxazine aerogel thermal protection composites for antioxidant ablation long to 1800 s. *Compos Part B—Eng* 2023, **266**: 111045.

[6] Savino R, Criscuolo L, Di Martino GD, *et al.* Aero-thermo–chemical

characterization of ultra-high-temperature ceramics for aerospace applications. *J Eur Ceram Soc* 2018, **38**: 2937–2953.
[7] Li CY, Gao RN, Ouyang HB, *et al.* Hierarchical porous ($Ta_{0.2}Nb_{0.2}Ti_{0.2}Zr_{0.2}Hf_{0.2}$)C high-entropy ceramics prepared by a self-foaming method for thermal insulation. *J Adv Ceram* 2024, **13**: 956–966.
[8] An ZM, Zhang RB, Fang DN. Synthesis of monolithic SiC aerogels with high mechanical strength and low thermal conductivity. *Ceram Int* 2019, **45**: 11368–11374.
[9] Shao JH, Bai CY, Li XY, *et al.* Open-cell mullite ceramic foams derived from porous geopolymer precursors with tailored porosity. *J Adv Ceram* 2023, **12**: 279–295.
[10] Sun JJ, Hu ZJ, Li JN, *et al.* Thermal and mechanical properties of fibrous zirconia ceramics with ultra-high porosity. *Ceram Int* 2014, **40**: 11787–11793.
[11] Bao KD, Huang YQ, Huang T, *et al.* Preparation of diatomite-based porous ceramics containing interlayer porous MgO by low-temperature sintering for integration of high strength and low thermal conductivity. *Mater Today Commun* 2024, **38**: 108028.
[12] Lin L, Xu J, Wang HC, *et al.* Near-net-size porous mullite ceramics with tuneable sintering shrinkage for thermal insulation applications. *Ceram Int* 2024, **50**: 9832–9839.
[13] Qin Z, Xu XJ, Xu TF, *et al.* High-strength thermal insulating porous mullite fiber-based ceramics. *J Eur Ceram Soc* 2022, **42**: 7209–7218.
[14] Xu CX, Hu R, Liu Y, *et al.* Research on preparation and related properties of macro–micro porous mullite ceramic skeletons via twice pore-forming technology. *RSC Adv* 2024, **14**: 12624–12632.
[15] Wang WJ, Cheng CF, Qiao JW, *et al.* Fabrication and mechanical properties of multi-principal cation (Mg,Ti,Cr,Zr,Al,Si) mullite ceramic. *Ceram Int* 2024, **50**: 25738–25748.
[16] Liang Y, Wang YQ, Qian JJ, *et al.* *In-situ* grown columnar mullite reinforced SiC porous ceramic membrane support with excellent mechanical performance and corrosion resistance: Using TiO_2 as the key to form columnar mullite. *Ceram Int* 2024, **50**: 44749–44761.
[17] Deng XG, Ran SL, Han L, *et al.* Foam-gelcasting preparation of high-strength self-reinforced porous mullite ceramics. *J Eur Ceram Soc* 2017, **37**: 4059–4066.
[18] Han S, Yang LW, Liu HT, *et al.* Micro-mechanical properties and interfacial engineering of SiC fiber reinforced sol–gel fabricated mullite matrix composites. *Mater Des* 2017, **131**: 265–272.
[19] Liu JX, Wan YG, Xiao B, *et al.* The preparation and performance analysis of zirconium-modified aluminum phosphate-based high-temperature (RT–1500 °C) resistant adhesive for joining alumina in extreme environment. *J Adv Ceram* 2024, **13**: 911–932.
[20] Li WH, Xu ZY, Tang HT, *et al.* Fabrication and characterization of mullite whiskers reinforced Al_2O_3–SiC–C castables. *J Alloys Compd* 2024, **1005**: 175931.
[21] Zhao PL, Ma SH, Wang XH, *et al.* Properties and mechanism of mullite whisker toughened ceramics. *Ceram Int* 2023, **49**: 10238–10248.
[22] Wang MC, Dong X, Zhou QJ, *et al.* An engineering ceramic-used high-temperature-resistant inorganic phosphate-based adhesive self-reinforced by *in situ* growth of mullite whiskers. *J Eur Ceram Soc* 2019, **39**: 1703–1706.
[23] He HT, Zhao R, Tian HY, *et al.* Sintering behavior of alumina whisker reinforced zirconia ceramics in hot oscillatory pressing. *J Adv Ceram* 2022, **11**: 893–900.
[24] Chen N, Wang HB, Huo JC, *et al.* Preparation and properties of *in situ* mullite whiskers reinforced aluminum chromium phosphate wave-transparent ceramics. *J Eur Ceram Soc* 2017, **37**: 4793–4799.
[25] He HT, Shao G, Zhao R, *et al.* Oscillatory pressure-assisted sinter forging for preparation of high-performance SiC whisker reinforced Al_2O_3 composites. *J Adv Ceram* 2023, **12**: 321–328.
[26] Chen PJ, Xiao P, Tang X, *et al.* Corrosion behavior and failure mechanism of SiC whisker and c-$AlPO_4$ particle-modified novel tri-layer $Yb_2Si_2O_7$/mullite/SiC coating in burner rig tests. *J Adv Ceram* 2022, **11**: 1901–1917.
[27] Li S, Zhang YM, Han JC, *et al.* Fabrication and characterization of SiC whisker reinforced reaction bonded SiC composite. *Ceram Int* 2013, **39**: 449–455.
[28] Wang MC, Li LY, Li ZY, *et al.* Mullite whiskers grown *in situ* reinforce a pre-ceramic resin adhesive for silicon carbide ceramics. *Ceram Int* 2019, **45**: 11131–11135.
[29] Lao D, Lin P, Liu XJ, *et al.* A novel approach to prepare high strength and high porosity reticulated porous ceramics by *in situ* synthesis of mullite whiskers. *Ceram Int* 2021, **47**: 14561–14568.
[30] Liu H, Xiong X, Li MH, *et al.* Fabrication and properties of mullite thermal insulation materials with *in situ* synthesized mullite hollow whiskers. *Ceram Int* 2020, **46**: 14474–14480.
[31] Li SH, Du HY, Guo AR, *et al.* Preparation of self-reinforcement of porous mullite ceramics through *in situ* synthesis of mullite whisker in flyash body. *Ceram Int* 2012, **38**: 1027–1032.
[32] Wang YH, Wang CH, You Y, *et al.* Finite element simulations of thermal stress distribution in thermal barrier coatings with different mullite whisker arrangements. *Ceram Int* 2024, **50**: 43397–43413.
[33] Yang MM, Li JJ, Man YR, *et al.* A novel hollow alumina sphere-based ceramic bonded by *in situ* mullite whisker framework. *Mater Des* 2020, **186**: 108334.
[34] Wang HL, Li SJ, Li YB, *et al.* Preparation of novel reticulated prickly porous ceramics with mullite whiskers. *J Eur Ceram Soc* 2021, **41**: 864–870.
[35] Chen XD, Li TH, Ren Q, *et al.* Mullite whisker network reinforced ceramic with high strength and lightweight. *J Alloys Compd* 2017, **700**: 37–42.
[36] Zhao HY, Li XL, Ji HM, *et al.* Constructing secondary-pore structure by *in situ* synthesized mullite whiskers to prepare whiskers aerogels with ultralow thermal conductivity. *J Eur Ceram Soc* 2019, **39**: 1344–1351.
[37] Yang N, Zhang RY, Qin T, *et al.* The effect of multiple factors on the synthesis of mullite whiskers based on the S–L–S mechanism and the comparison of strengthening performance. *J Alloys Compd* 2024, **997**: 174947.
[38] Yang JJ, Zhang XY, Zhang BR, *et al.* Mullite ceramic foams with tunable pores from dual-phase sol nanoparticle-stabilized foams. *J Eur Ceram Soc* 2022, **42**: 1703–1711.
[39] Ren B, Kang SJ, Liu JJ, *et al.* Low-temperature preparation of alumina–mullite porous ceramic via gelation-assisted dual-phasic nanoparticle stabilized foams. *Ceram Int* 2024, **50**: 29428–29436.
[40] Li CW, Bian C, Han Y, *et al.* Mullite whisker reinforced porous anorthite ceramics with low thermal conductivity and high strength. *J Eur Ceram Soc* 2016, **36**: 761–765.
[41] Li XX, Yan LW, Zhang YB, *et al.* Lightweight porous silica ceramics with ultra-low thermal conductivity and enhanced compressive strength. *Ceram Int* 2022, **48**: 9788–9796.
[42] Zhu ZW, Wei ZL, Shen JX, *et al.* Fabrication and catalytic growth mechanism of mullite ceramic whiskers using molybdenum oxide as catalyst. *Ceram Int* 2017, **43**: 2871–2875.
[43] Bella ML, Hamidouche M, Gremillard L. Preparation of mullite-alumina composite by reaction sintering between Algerian kaolin and amorphous aluminum hydroxide. *Ceram Int* 2021, **47**: 16208–16220.
[44] Wang X, Guo AR, Liu JP, *et al.* Effects of *in situ* synthesized mullite whiskers on compressive strength of mullite fiber brick. *Ceram Int* 2016, **42**: 13161–13167.
[45] Zhou LJ, Li ZH, Zhu YM. Porous silica/mullite ceramics prepared by foam-gelcasting using silicon kerf waste as raw material. *Mater Lett* 2019, **239**: 67–70.
[46] Zhu JX, Zhu RJ, Hu YW, *et al.* Mullite fiber porous ceramic with high quality factor for high-temperature PM filtration. *J Eur Ceram Soc* 2024, **44**: 2630–2637.
[47] Cha HA, Jo MG, Moon YK, *et al.* Highly porous YSZ ceramic foams using hollow spheres with holes in their shell for high-performance thermal insulation. *J Eur Ceram Soc* 2023, **43**: 7041–7052.
[48] Huang Y, Hu NY, Ye YC, *et al.* A novel route for the fabrication of

melilite-spinel porous ceramics with ultralow thermal conductivity and sufficient strength. *Ceram Int* 2022, **48**: 37488–37491.
[49] Ren YH, Zhang B, Ye J, *et al.* Preparation of porous Y_2SiO_5 ceramics with high porosity and extremely low thermal conductivity for radome applications. *Ceram Int* 2023, **49**: 2394–2400.
[50] Jia T, Chen H, Dong X, *et al.* Preparation of homogeneous mullite fibrous porous ceramics consolidated by propylene oxide. *Ceram Int* 2019, **45**: 2474–2482.
[51] Chen H, Xiang HM, Dai FZ, *et al.* Porous high entropy $(Zr_{0.2}Hf_{0.2}Ti_{0.2}Nb_{0.2}Ta_{0.2})B_2$: A novel strategy towards making ultrahigh temperature ceramics thermal insulating. *J Mater Sci Technol* 2019, **35**: 2404–2408.
[52] Yang FY, Zhao S, Sun WC, *et al.* Fibrous porous mullite ceramics modified by mullite whiskers for thermal insulation and sound absorption. *J Eur Ceram Soc* 2023, **43**: 521–529.
[53] Hou XH, Liu ZL, Liu ZQ, *et al.* Porous fibrous ZrO_2–mullite ceramics prepared via tert-butyl alcohol-based gel-casting. *Ceram Int* 2018, **44**: 13580–13587.
[54] Yang YL, Fu WY, Chen XX, *et al.* Fabrication of homogeneous mullite-based fiber porous ceramics with high strength and porosity. *J Eur Ceram Soc* 2022, **42**: 7219–7227.
[55] Zhang J, Dong X, Hou F, *et al.* Effects of fiber length and solid loading on the properties of lightweight elastic mullite fibrous ceramics. *Ceram Int* 2016, **42**: 5018–5023.
[56] Wang XY, Hu ZJ, Sun CC, *et al.* Fibrous porous ceramics with devisable phenolic resin reinforcing layer. *Ceram Int* 2019, **45**: 5413–5417.
[57] Yuan L, Ma BY, Zhu Q, *et al.* Preparation and properties of mullite-bonded porous fibrous mullite ceramics by an epoxy resin gel-casting process. *Ceram Int* 2017, **43**: 5478–5483.
[58] Zhang RB, Ye CS, Hou XB, *et al.* Microstructure and properties of lightweight fibrous porous mullite ceramics prepared by vacuum squeeze moulding technique. *Ceram Int* 2016, **42**: 14843–14848.
[59] Dong X, Sui GF, Liu JC, *et al.* Mechanical behavior of fibrous ceramics with a bird's nest structure. *Compos Sci Technol* 2014, **100**: 92–98.
[60] Hu XZ. Additive effect of micro-damage zones from nano-scale crack tip and nano-grains for fracture toughness measurements of 3Y-TZP zirconia ceramics. *J Eur Ceram Soc* 2022, **42**: 7174–7179.
[61] Wu JT, Chen HY, Luo X, *et al.* Design, fabrication, microstructure, and properties of highly porous alumina whisker foam ceramic. *Ceram Int* 2022, **48**: 2776–2781.
[62] Yuan L, Liu ZL, Hou XH, *et al.* Fibrous ZrO_2–mullite porous ceramics fabricated by a hydratable alumina based aqueous gel-casting process. *Ceram Int* 2019, **45**: 8824–8831.
[63] Zhou WY, Zhang Z, Li N, *et al.* Effect of the *in situ* SiC whiskers on the alkali attack resistance mechanism of mullite–SiC foam ceramics. *Ceram Int* 2023, **49**: 22932–22940.
[64] Ibrahim JEFM, Kurovics E, Tihtih M, *et al.* Reaction synthesis of porous nano-structured mullite ceramic composites from alumina and zeolite-poor rock with enhanced strength and low thermal conductivity. *Results Eng* 2023, **20**: 101423.
[65] Suchanicz J, Kruzina TV. Dielectric properties, thermal expansion and heat capacity of $(1-x)Na_{0.5}Bi_{0.5}TiO_3$–$xBaTiO_3$ single crystals (x = 0, 0.02, 0.025, 0.0325 and 0.05). *Mater Sci Eng B* 2013, **178**: 889–895.
[66] Gu XH, Fan AY, Liu SW, *et al.* Molybdenum oxide catalyzed low temperature preparation of mullite whisker from silica-alumina gel slag. *J Mater Res Technol* 2024, **32**: 1449–1459.
[67] Chen AB, Li L, Ren WL, *et al.* Enhancing thermal insulation and mechanical strength of porous ceramic through size-graded MA hollow spheres. *Ceram Int* 2023, **49**: 33247–33254.
[68] Xu GG, Ma YH, Cui HZ, *et al.* Preparation of porous mullite–corundum ceramics with controlled pore size using bioactive yeast as pore-forming agent. *Mater Lett* 2014, **116**: 349–352.
[69] Li X, Li S, Wan YM, *et al.* Controllable preparation and properties of gel-casting porous mullite ceramics via lignin fiber assisted pore formation method. *Ceram Int* 2023, **49**: 35552–35562.
[70] Yan XH, Yuan L, Liu ZL, *et al.* Preparation of porous mullite ceramic for high temperature flue gas filtration application by gel casting method. *J Aust Ceram Soc* 2021, **57**: 1189–1198.
[71] Okada K, Uchiyama S, Isobe T, *et al.* Capillary rise properties of porous mullite ceramics prepared by an extrusion method using organic fibers as the pore former. *J Eur Ceram Soc* 2009, **29**: 2491–2497.
[72] Hossain SKS, Pyare R, Roy PK. Synthesis of *in situ* mullite foam using waste rice husk ash derived Sol by slip-casting route. *Ceram Int* 2020, **46**: 10871–10878.
[73] Vijayan S, Wilson P, Prabhakaran K. Ultra low-density mullite foams by reaction sintering of thermo-foamed alumina–silica powder dispersions in molten sucrose. *J Eur Ceram Soc* 2017, **37**: 1657–1664.
[74] Choo TF, Salleh MAM, Kok KY, *et al.* Modified cenospheres as non-sacrificial pore-forming agent for porous mullite ceramics. *Ceram Int* 2019, **45**: 21827–21834.
[75] Bai JH. Fabrication and properties of porous mullite ceramics from calcined carbonaceous Kaolin and α-Al_2O_3. *Ceram Int* 2010, **36**: 673–678.
[76] Guo HS, Ye FB, Li WF, *et al.* Preparation and characterization of foamed microporous mullite ceramics based on kyanite. *Ceram Int* 2015, **41**: 14645–14651.
[77] Liu DZ, Hu P, Zhao GD, *et al.* Silica bonded mullite fiber composite with isotropic geometry and properties for thermal insulating. *J Alloys Compd* 2017, **728**: 1049–1057.
[78] Zhou XZ, Zhu SF, Wang YX, *et al.* Preparation of porous mullite–corundum ceramics via organic foam impregnation. *Korean J Mater Res* 2022, **32**: 85–93.